Journal of the Meteorological Society of Japan

EARLY ONLINE RELEASE

The DOI for this manuscript is
DOI:10.2151/jmsj.2021-076
J-STAGE Advance published date: September 14th, 2021
The final manuscript after publication will replace the preliminary version at the above DOI once it is available.

Variational data assimilation system for operational regional models at Japan Meteorological Agency

Yasutaka IKUTA

Meteorological Research Institute, Tsukuba, Japan

and

Tadashi FUJITA

Meteorological Research Institute, Tsukuba, Japan

Yukinari OTA

Numerical Prediction Development Center, Japan Meteorological Agency, Tsukuba, Japan

Yuki HONDA

Japan Meteorological Agency, Tokyo, Japan

September 1, 2021

Corresponding author: Yasutaka IKUTA, Department of Observation and Data Assimilation, Meteorological Research Institute, Japan Meteorological Agency, 1-1 Nagamine, Tsukuba, Ibaraki 305-0052, Japan.
E-mail: yasutaka.ikuta@mri-jma.go.jp

Abstract

The regional data assimilation system at the Japan Meteorological Agency employs a variational data assimilation system on the basis of the non-hydrostatic model ASUCA (named ASUCA-Var). This paper reviews configurations and the current status of ASUCA-Var. To consider the consistency of analysis and prognostic variables, the control variables of ASUCA-Var include soil variables and basic atmospheric variables. The background-errors based on the control variables are calculated every three hours for land and sea grid points to better reflect the representative error covariance structure, taking into account daily variations and differences in structure on land and sea. Although the cost function is designed to be a perfect quadratic form, the basic field update method in the optimization process allows the nonlinearity of the observation operator and numerical weather prediction model to be incorporated into the solution of optimization problem in the incremental four-dimensional variational (4D-Var) method. The outer/inner models used in the incremental 4D-Var method are based on ASUCA, with suitable configurations according to each resolution and applied linearization. Observation operators are implemented for various kinds of observations used, with unified interfaces encapsulating external simulators. Variational quality control and variational bias correction are also introduced for advanced observation handling within the variational system.

Parallelization is introduced to enhance computational efficiency, including adjoint calculations. To assess the impact of assimilated observations, degrees of freedom for signal are also available. In addition, as a system for operational use, ASUCA-Var is designed for sustainable development. The meso-scale analysis and local analysis workflows are presented as operational implementations of ASUCA-Var. ASUCA-Var improves forecasting in a wide range of validation indices. The major future improvements of ASUCA-Var include the introduction of the flow-dependent background-error and the extension of the control variable to hydrometeors, which are expected to enhance the prediction accuracy of the operational regional model.

Keywords Data assimilation; Mesoscale; Numerical Weather Prediction; Operational system; Variational method;

1. Introduction

The first study which used the variational method to generate initial conditions for numerical forecast models was conducted by Sasaki (1958). Thereafter, the adjoint method studied theoretically by Talagrand and Courtier (1987) paved the way for the practical application of four-dimensional variational methods. Parrish and Derber (1992) documented the first success with the operational use of the three-dimensional variational (3D-Var) data assimilation method in numerical weather prediction (NWP) for finding an optimal solution in a three-dimensional atmosphere. The practical application of a four-dimensional variational (4D-Var) data assimilation method, which includes the time component in the cost function, was introduced through the advent of the incremental 4D-Var (Courtier et al., 1994), which had its first operational run at the European Centre for Medium-Range Weather Forecasts in 1997 (Rabier et al., 2000; Mahfouf and Rabier, 2000; Klinker et al., 2000). Since then, variational data assimilation has made rapid progress both in its methodology and its extensive use of observations at NWP centers, serving as a foundation of high-quality weather prediction across a wide range of forecast time periods and spatial resolution.

An important objective in NWP is to forecast severe weather events localized in time and space using a high-resolution limited-area model, and the enhancement of data assimilation systems is one of the key elements to achieve this. Gustafsson et al. (2018) comprehensively reviewed convection-scale data assimilation systems for NWP centers worldwide, including Japan. Variational data assimilation methods are essential for regional NWP and have been used by Météo-France, the HIgh-Resolution Limited-Area Modeling (HIRLAM) consortium, the Aire Limitée Adaptation dynamique Développement InterNational (ALADIN) consortium, the Regional Cooperation for Limited-Area modeling in Central Europe (RC LACE) consortium, the National Oceanic and Atmospheric Administration of the USA (NOAA), the Met Office, and the Japan Meteorological Agency (JMA) in their operational systems to create initial conditions for regional models (Gustafsson et al., 2018).

As of 2021, JMA has been operating two regional NWP models, one is the Meso-Scale Model (MSM) with a resolution of 5 km and the other is the Local Forecast Model (LFM) with a resolution of 2 km, both based on the non-hydrostatic model ASUCA (Ishida et al., 2009, 2010; Hara et al., 2012) and the recent updates are reported by the outline of NWP at JMA (Japan Meteorological Agency, 2019) and Ikuta et al. (2020). The operational data assimilation (DA) systems for pre-processing and quality control of observational data, known as meso-scale analysis (MA) for MSM and local analysis (LA) for LFM, have shared the core of the variational DA system based on ASUCA (ASUCA-Var).

JMA started to use 4D-Var for regional NWP to initialize the hydrostatic MSM in March 2002 (Ishikawa and Koizumi, 2002), called Meso-4DVar, which was the world's first 'regional' 4D-Var system. Afterwards, the MSM forecast model was updated to the JMA Non-Hydrostatic Model (JMA-NHM; Saito et al., 2006, 2007) in 2004, followed by updating the DA system to the 'JMA Non-hydrostatic model'-based four-dimensional Variational data Assimilation system (JNoVA; Honda et al., 2005; Honda and Sawada, 2009, 2010) in April 2009. In January 2017, ASUCA was introduced to the MSM replacing JMA-NHM. In March 2020, ASUCA-4DVar was introduced for MA applying a consistent DA system to the forecast model (Ikuta et al., 2020).

Besides operational usage, these systems have been beneficial for research purposes. For instance, the Meso-4DVar was used to investigate assimilation impacts of precipitable water vapor (PWV) data derived by Global Positioning System (GPS), radial wind vectors derived by Doppler radar (Seko et al., 2004), GPS-PWV data (Shoji et al., 2011), and GPS radio occultation refractivity (Kunii et al., 2012). JNoVA was used to demonstrate a state-of-the-art NWP with the first regional reanalysis of Typhoon

Vera which occurred in 1959 (Kawabata et al., 2012) and also to demonstrate the improved forecasting accuracy of extreme event with hybrid-4DVar (Ito et al., 2016). Another research 4D-Var system closely related to JNoVA is NHM-4DVAR, which is a cloud-resolving non-hydrostatic 4D-Var used in several studies (e.g., Kawabata et al., 2007, 2011, 2014).

Conversely, LFM has been operationally introduced in 2012, using JMA-NHM as the forecast model, and applying the 3D-Var version of JNoVA in LA. These were replaced by ASUCA and ASUCA-3DVar in January 2015 (Aranami et al., 2015), followed by an upgrade of ASUCA-3DVar to begin assimilation of the clear sky radiance and the soil moisture from satellite data, and to introduce variational bias correction in January 2017 (Ikuta, 2017a).

ASUCA-Var was created from scratch following the update of the forecast model from JMA-NHM to ASUCA, and pre-processing also was reconstructed to adapt to this new assimilation system. In developing the DA system, coding rules and design strategies were reviewed by developers to maintain a schedule to keep the system up to date, which is one of the main requisites in operating an adjoint-based method for a sustainable development. Although there was no novelty in the light of science to the reconstruction with widely proven technology, it was conducted with careful design reviews and several refinements and the system has strongly enhanced the efficiency of development leading to the improvement of prediction accuracy. Consequently, ASUCA-Var was brought into operation in the LA in 2015 as version LA1501 and then in the MA in 2020 as version MA2003. These systems are now mature and will proceed toward variational data assimilation with ensemble method in the future. Thus, it is timely to review the current state of operational regional DA techniques at JMA.

In this review paper, first, we describe the formulation of the ASUCA-Var variational data assimilation method, including cost function, background error, observation operator, and model operator terms; the concept of design for sustainable development and parallelization are shown in Section 2. In Section 3, operational systems are introduced. In Section 4, the performance of ASUCA-Var is demonstrated. The conclusion and future plans are described in the last section.

2. Variational data assimilation method

ASUCA-Var is a core system of LA and MA that uses 3D-Var and 4D-Var, respectively. The fundamental formulation is common to both systems, and 3D-Var can be seen as a simplified method of 4D-Var. Hence, this section details the 4D-Var version of ASUCA-Var, and the configuration of MA and LA will be described in Section 3.

2.1 *Cost function*

a. Formulation

In the variational DA method, the analysis value is obtained by minimizing the cost function. The cost function of ASUCA-Var is defined as

$$J = J^{\mathrm{b}} + J^{\mathrm{o}} + J^{\mathrm{bc}} + J^{\mathrm{df}}, \tag{1}$$

where J^{b} is a background term to measure the distance of the unknown model state from the background state, J^{o} is an observation term to measure the distance of the unknown model state from the observations, J^{bc} is a variational bias correction (VarBC; Dee, 2004; Cameron and Bell, 2018) term to estimate observation bias, and J^{df} is a penalty term to reduce the gravity wave as noise using a digital filter (DF; e.g., Gustafsson, 1992; Lynch, 1997; Gauthier and Thépaut, 2001; Wee and Kuo, 2004).

First, the background term J^{b} is given as

$$J^{\mathrm{b}} = \frac{1}{2}\left(\mathbf{x}_0 - \mathbf{x}_0^{\mathrm{b}}\right)^{\mathrm{T}} \mathbf{B}_0^{-1} \left(\mathbf{x}_0 - \mathbf{x}_0^{\mathrm{b}}\right), \tag{2}$$

where $\mathbf{x}_0$ is the state vector at time t_0, $\mathbf{x}_0^{\mathrm{b}}$ is the state vector of the first guess at time t_0, $\mathbf{B}_0$ is the background error covariance matrix, and t_0 is the start time of assimilation window. $\mathbf{B}_0$ is constructed assuming that the error distribution is Gaussian, and is given as a positive definite symmetric matrix by prior statistics investigation (subsection 2.7). In this paper, we solve the problem under the assumption where $\mathbf{B}_0^{-1}$ exists following the formulation of traditional variational methods, and refer to Ide et al. (1997) for notation.

Second, the observation term J^{o} measures the distance of the unknown model state from observations y_i^{o} at observed time t_i. An observation operator $\mathcal{H}_i$ to compute the model state corresponding to observation state at t_i is described as

$$\mathcal{H}_i\left(\mathbf{x}_i\right)=\mathcal{H}_i\left(\mathcal{M}_{i,0}\left(\mathbf{x}_0\right)\right), \tag{3}$$

where $\mathcal{M}_{i,0}$ is the nonlinear model operator based on ASUCA. The role of $\mathcal{M}_{i,0}$ is the time propagation from $\mathbf{x}_0$ to $\mathbf{x}_i$ as

$$\mathbf{x}_i=\mathcal{M}_{i,0}\left(\mathbf{x}_0\right). \tag{4}$$

Using those operators, J^{o} is given as

$$J^{\mathrm{o}}=\sum_{i=0}^{n}\frac{1}{2}\left(\mathcal{H}_i\left(\mathcal{M}_{i,0}\left(\mathbf{x}_0\right)\right)-\mathbf{y}_i^{\mathrm{o}}+\mathcal{P}\left(\boldsymbol{\beta}\right)\right)^{\mathrm{T}}\mathbf{R}_i^{-1}\left(\mathcal{H}_i\left(\mathcal{M}_{i,0}\left(\mathbf{x}_0\right)\right)-\mathbf{y}_i^{\mathrm{o}}+\mathcal{P}\left(\boldsymbol{\beta}\right)\right), \tag{5}$$

where $\mathcal{P}\left(\boldsymbol{\beta}\right)$ is observation bias, $\mathbf{R}_i$ is the observation error covariance matrix, and $[t_0, t_n]$ is the range of the assimilation window.

Third, the VarBC term J^{bc} to estimate the observation bias is given as

$$J^{\mathrm{bc}}=\frac{1}{2}\left(\boldsymbol{\beta}-\boldsymbol{\beta}^{\mathrm{b}}\right)^{\mathrm{T}}\mathbf{B}_{\mathrm{bc}}^{-1}\left(\boldsymbol{\beta}-\boldsymbol{\beta}^{\mathrm{b}}\right), \tag{6}$$

where $\boldsymbol{\beta}$ is a control variable for bias correction, $\boldsymbol{\beta}^{\mathrm{b}}$ is the first guess of $\boldsymbol{\beta}$, and $\mathbf{B}_{\mathrm{bc}}$ is the background error covariance matrix for VarBC. The VarBC is only applied to satellite observations in our operational system (see subsection 2.5).

Finally, the penalty term J^{df} is given as

$$J^{\mathrm{df}} = \frac{1}{2}\left(\sum_{k=0}^{N}\gamma_k\mathcal{M}_{k,0}\left(\mathbf{x}_0\right)\right)^{\mathrm{T}}\mathbf{B}_{\mathrm{df}}^{-1}\left(\sum_{k=0}^{N}\gamma_k\mathcal{M}_{k,0}\left(\mathbf{x}_0\right)\right), \tag{7}$$

where γ_k and $\mathbf{B}_{\mathrm{df}}$ are weighting coefficients at the k-th timestep ($k = 0, \cdots, N$) and a diagonal matrix for DF, respectively; see subsection 2.6.

b. Basic field update

Solving the problem of minimizing the linearized cost function yields the analysis value. By expanding the cost function around the basic field, the problem to be solved is transformed into a complete quadratic form, allowing for stable numerical calculations. Here the basic field refers to the trajectory of the model variables given by the nonlinear model in the model space. Because optimization is based on linear theory, it was not possible to incorporate the effects of nonlinear processes, but the basic field update (Trémolet, 2008) alleviated this problem and allowed the effects of nonlinear processes to be included in optimization.

For the basic field update, the basic field at the first iteration is equal to the trajectory of the first guess. After minimizing the cost function to obtain the analysis value (inner loop), the basic field is recalculated from the analysis value using a nonlinear NWP model. The newly calculated basic field is used to re-linearize and minimize the cost function for the next iteration. This iterative updating and minimization of the basic field yields the final analysis value. Such cycles of the basic field computation and the inner loop are called the outer loop. The specific procedure of the basic field update in MA is explained in Section 3. Briefly, the outer loop is repeated three times in MA. The first inner loop has 20 iterations, and the second and third inner loops have 15 iterations each. The basic field is updated twice at the connection of inner loops.

The cost function linearized around the j-th basic field based on Trémolet (2008) is defined as follows:

$$J^{\mathrm{b}} = \frac{1}{2}\left(\delta\mathbf{x}_0^{(j)} - \delta\mathbf{x}_0^{\mathrm{b}(j)}\right)^{\mathrm{T}} \mathbf{B}_0^{-1}\left(\delta\mathbf{x}_0^{(j)} - \delta\mathbf{x}_0^{\mathrm{b}(j)}\right), \tag{8}$$

$$J^{\mathrm{o}} = \frac{1}{2}\sum_{i=0}^{n}\left(\mathbf{H}_i^{(j)}\mathbf{M}_{i,0}^{(j)}\delta\mathbf{x}_0^{(j)} + \mathbf{P}^{(j)}\delta\boldsymbol{\beta}^{(j)} - \mathbf{d}_i^{(j)}\right)^{\mathrm{T}} \mathbf{R}_i^{-1}\left(\mathbf{H}_i^{(j)}\mathbf{M}_{i,0}^{(j)}\delta\mathbf{x}_0^{(j)} + \mathbf{P}^{(j)}\delta\boldsymbol{\beta}^{(j)} - \mathbf{d}_i^{(j)}\right), \tag{9}$$

$$J^{\mathrm{bc}} = \frac{1}{2}\left(\delta\boldsymbol{\beta}^{(j)} - \delta\boldsymbol{\beta}^{\mathrm{b}(j)}\right)^{\mathrm{T}} \mathbf{B}_{\mathrm{bc}}^{-1}\left(\delta\boldsymbol{\beta}^{(j)} - \delta\boldsymbol{\beta}^{\mathrm{b}(j)}\right), \tag{10}$$

$$J^{\mathrm{df}} = \frac{1}{2}\left(\boldsymbol{\Gamma}^{(j)}\delta\mathbf{x}_0^{(j)} - \mathbf{g}^{(j)}\right)^{\mathrm{T}} \mathbf{B}_{\mathrm{df}}^{-1}\left(\boldsymbol{\Gamma}^{(j)}\delta\mathbf{x}_0^{(j)} - \mathbf{g}^{(j)}\right), \tag{11}$$

where j is the number of iterations of the basic field update, and the number of iterations in inner loop is omitted to avoid complexity. For example, the basic field update with $j = 1$ is conducted after the first 20 iterations. The details of the cost function will be described below. The j-th increment

$\delta\mathbf{x}_0^{(j)}$ is given as

$$\delta\mathbf{x}_0^{(j)} = \mathbf{x}_0 - \mathbf{x}_0^{(j-1)}, \tag{12}$$

and the j-th difference of the background is given as

$$\delta\mathbf{x}_0^{\mathrm{b}(j)} = \mathbf{x}_0^{\mathrm{b}} - \mathbf{x}_0^{(j-1)}, \tag{13}$$

where $\mathbf{x}_0^{(j)}$ is the basic field at the j-th update. Similarly, the increments for VarBC are defined as

$$\delta\boldsymbol{\beta}^{(j)} = \boldsymbol{\beta} - \boldsymbol{\beta}^{(j-1)}, \tag{14}$$

$$\delta\boldsymbol{\beta}^{\mathrm{b}(j)} = \boldsymbol{\beta}^{\mathrm{b}} - \boldsymbol{\beta}^{(j-1)}. \tag{15}$$

The basic field for the initial iteration $j = 1$ is the same as the first guess $\mathbf{x}_0^{\mathrm{g}}$ and $\boldsymbol{\beta}^{\mathrm{g}}$:

$$\mathbf{x}_0^{(0)} = \mathbf{x}_0^{\mathrm{g}}, \tag{16}$$

$$\boldsymbol{\beta}^{(0)} = \boldsymbol{\beta}^{\mathrm{g}}. \tag{17}$$

$\mathbf{x}_0^{\mathrm{g}}$ is given by the forecast from the previous analysis, and $\boldsymbol{\beta}^{\mathrm{g}}$ is succeeded from the previous analysis.

The tangent-linear operators $\mathbf{H}_i^{(j)}$, $\mathbf{M}_{i,0}^{(j)}$, and $\mathbf{P}^{(j)}$ are obtained by tangent linearizing the nonlinear operators $\mathcal{H}_i$, $\mathcal{M}_{i,0}$, and $\mathcal{P}$ around the basic field $\mathbf{x}_0^{(j-1)}$ and $\boldsymbol{\beta}^{(j-1)}$. The relationships of nonlinear operators and tangent-linear operators are written as

$$\mathcal{H}_i\left(\mathbf{x}_i^{(j-1)} + \delta\mathbf{x}_i^{(j)}\right) = \mathcal{H}_i\left(\mathbf{x}_i^{(j-1)}\right) + \mathbf{H}_i^{(j)}\delta\mathbf{x}_i^{(j)}, \tag{18}$$

$$\mathcal{M}_{i,0}\left(\mathbf{x}_0^{(j-1)} + \delta\mathbf{x}_0^{(j)}\right) = \mathcal{M}_{i,0}\left(\mathbf{x}_0^{(j-1)}\right) + \mathbf{M}_{i,0}^{(j)}\delta\mathbf{x}_0^{(j)}, \tag{19}$$

$$\mathcal{P}\left(\boldsymbol{\beta}^{(j-1)} + \delta\boldsymbol{\beta}^{(j)}\right) = \mathcal{P}\left(\boldsymbol{\beta}^{(j-1)}\right) + \mathbf{P}^{(j)}\delta\boldsymbol{\beta}^{(j)}, \tag{20}$$

where we ignore the second order and higher order terms on the right-hand side. The matrix elements of the tangent-linear operators in Eqs. (18)–(20) are replaced by the basic field update. The j-th innovation is given as

$$\mathbf{d}_i^{(j)} = \mathbf{d}_i + \mathcal{H}_i\left(\mathcal{M}_{i,0}\left(\mathbf{x}_0^{\mathrm{g}}\right)\right) - \mathcal{H}_i\left(\mathcal{M}_{i,0}\left(\mathbf{x}_0^{(j-1)}\right)\right) + \mathcal{P}\left(\boldsymbol{\beta}^{\mathrm{g}}\right) - \mathcal{P}\left(\boldsymbol{\beta}^{(j-1)}\right), \tag{21}$$

using the nonlinear operators. In the incremental approach, the model operator used to calculate the cost function in the iteration is a low-resolution model $\mathcal{M}_{i,0}$, and $\mathbf{d}_i \left(= \mathbf{y}_i^{\mathrm{o}} - \mathcal{H}_i\left[\mathcal{M}_{i,0}^{\mathrm{h}}\left(\mathbf{x}_0^{\mathrm{g}}\right)\right] - \mathcal{P}\left(\boldsymbol{\beta}^{\mathrm{g}}\right)\right)$ is an innovation estimated with a high-resolution model $\mathcal{M}_{i,0}^{\mathrm{h}}$ which is invariant in the optimization and independent of basic field updates. Additionally, the first guess $(\cdot)^{\mathrm{g}}$ is used for the background state $(\cdot)^{\mathrm{b}}$.

The model operator in the DF term is linearized around the basic field. The weighted average of the basic field trajectory is given as

$$\mathbf{g}^{(j)} = \sum_{k=0}^{N}\gamma_k\mathcal{M}_{k,0}\left(\mathbf{x}_0^{(j-1)}\right), \tag{22}$$

and the perturbation around the basic field trajectory is given as

$$\sum_{k=0}^{N}\gamma_k\mathcal{M}_{k,0}\left(\mathbf{x}_0^{(j-1)} + \delta\mathbf{x}_0^{(j)}\right) = \mathbf{g}^{(j)} + \boldsymbol{\Gamma}^{(j)}\delta\mathbf{x}_0^{(j)}, \tag{23}$$

where the tangent-linear operator for the DF is defined as

$$\mathbf{\Gamma}^{(j)} = \sum_{k=0}^{N} \gamma_k \mathbf{M}_{k,0}^{(j)}. \tag{24}$$

Because of the limitation of computation time in operational runs, as mentioned earlier, the number of basic field updates in the MA was set to two, with the three-time inner loops (20, 15, and 15 iterations). For forecasting heavy rain events, which are greatly affected by nonlinear processes in NWP models, the accuracy can be improved if the number of basic field updates is increased.

2.2 Analysis variables

The elements selected for variational optimization are described as

$$x_0 = \left(u, v, T_\mathrm{g}, P_\mathrm{s}, \theta, W_\mathrm{g}, \mu_\mathrm{p}\right), \tag{25}$$

at assimilation window start time ($t = t_0$). The descriptions of these elements are given in the following list:

- u (m s^{-1}), x axis wind component;
- v (m s^{-1}), y axis wind component;
- T_g (K), soil temperature;
- P_s (Pa), surface pressure;

- θ (K), potential temperature;
- W_{g} (unitless), soil volumetric water content;
- μ_{p} (unitless), pseudo relative humidity.

μ_{p} is defined as $\mu_{\mathrm{p}} = q_{\mathrm{v}}/q_{\mathrm{sat}}^{\mathrm{b}}$ (Dee and da Silva, 2003), where q_{v} (kg kg^{-1}) is the mixing ratio of water vapor, $q_{\mathrm{sat}}^{\mathrm{b}}$ (kg kg^{-1}) is saturated water vapor fixed by the first guess value. μ_{p} has a greater benefit compared with q_{v}, being closer to Gaussian-shaped error distributions. These elements are not the same as the prognostic variables in the forecast model. The prognostic variables of the model are derived from these analysis variables in Eq. (25). However, both hydrometeors and the vertical velociy are not included in the set of analysis variables and are initialized with the first guess values and zero, respectively, at the assimilation window start time.

The space to be optimized by data assimilation is discretized into cubic cells using the finite volume method, the same as ASUCA. The vector variables u and v are placed at the centers of the sides of the cell (u-point and v-point). Thus, they are staggered in the grid representation. The scalar variable is placed at the center of the cell (p-point), and its value is the cell average.

2.3 *Background term*

The background term measures the distance between the unknown model state and the first guess as the background state. The distance is normalized by the background error covariance matrix $\mathbf{B}_0$, which is defined by the statistical error of the background state $\mathbf{x}_0^{\mathrm{b}}$ from the true state $\mathbf{x}_0^{\mathrm{t}}$ at $t = t_0$. $\mathbf{B}_0$ is given as

$$\mathbf{B}_0 = \left\langle \left(\mathbf{x}_0^{\mathrm{b}} - \mathbf{x}_0^{\mathrm{t}}\right), \left(\mathbf{x}_0^{\mathrm{b}} - \mathbf{x}_0^{\mathrm{t}}\right)^{\mathrm{T}} \right\rangle, \tag{26}$$

where $\langle\cdot\rangle$ indicates the expectation value (e.g., Bannister, 2008). The number of dimensions of the full $\mathbf{B}_0$ is huge, approximately $10^9 \times 10^9$ as estimated by the degrees of freedom of MSM, that it is difficult to practically calculate. By assuming that some variables are uncorrelated and making the background error covariance matrix sparse, the calculation cost can be significantly reduced. For simplicity, we omit the error correlations between some of the elements and divide $\mathbf{B}_0$ into four blocks as follows:

$$\mathbf{B}_0 = \begin{pmatrix} \mathbf{B}_u & 0 & 0 & 0 \\ 0 & \mathbf{B}_v & 0 & 0 \\ 0 & 0 & \mathbf{B}_{T_{\mathrm{g}},P_{\mathrm{s}},\theta} & 0 \\ 0 & 0 & 0 & \mathbf{B}_{W_{\mathrm{g}},\mu_{\mathrm{p}}} \end{pmatrix}, \tag{27}$$

where the background error of u and v are independent of other elements, the background errors of T_{g}, P_{s}, and θ are assumed to be correlated, and this is also the case for W_{g} and μ_{p}. In our system, the error correlation between the potential temperature and the wind velocities is ignored because it is statistically smaller than the other error correlations. This assumption facilitates the modeling of error covariance and can reduce the computational cost of the optimization. The background error is estimated by the National Meteorological Center (NMC) method (Parrish and Derber, 1992). The NMC method estimates the background error using the difference between the 6-hour forecast $\mathbf{x}^{\mathrm{f}}\,(t=6\mathrm{h})$ and the 3-hour forecast $\mathbf{x}^{\mathrm{f}}\,(t=3\mathrm{h})$ at the same valid time, as follows:

$$\hat{\mathbf{B}} = \alpha \left\langle \left(\mathbf{x}^{\mathrm{f}}\,(t=6\mathrm{h}) - \mathbf{x}^{\mathrm{f}}\,(t=3\mathrm{h})\right), \left(\mathbf{x}^{\mathrm{f}}\,(t=6\mathrm{h}) - \mathbf{x}^{\mathrm{f}}\,(t=3\mathrm{h})\right)^{\mathrm{T}} \right\rangle, \quad (28)$$

where α is a scaling factor. The 3 h difference is due to the 3 h data assimilation window. In the actual calculation, both $\mathbf{x}^{\mathrm{f}}\,(t=6\mathrm{h})$ and $\mathbf{x}^{\mathrm{f}}\,(t=3\mathrm{h})$ are calculated using the same lateral-boundary condition. This method is called the lagged NMC method (Široká et al., 2003) and eliminates the source of error which comes from the lateral-boundary condition. We assume that the vertical background error is independent of the horizontal background error. Horizontal background error correlations are independent between the x and y directions. The shape of the horizontal background error correlation is given in Gaussian form. The statistics data are taken as the 10^{th}–19^{th} of each month from March 2018 to February 2019. The background error was calculated separately for land and sea grid points and classified by 3-hourly local time.

The scaling factor α was adjusted to match the new background error variance with the previous operational variance at about 500 hPa, keeping a balance between background error and observation error. Figure 1 shows the variance profiles on land and sea grid points. Horizontal winds u and v have large variance inside the boundary layer at night on the land grid points and small variance during the daytime when vertical convection mixing is strong. Conversely, the variance of horizontal winds over the sea has negligible time dependency. The variance of ground temperature and potential temperature is large on the land grid point and small on the sea grid point. The bottom-level variances of T_{g} and W_{g} are zero because the climate values are given as boundary conditions in the forecast model. Figure 2 shows the error correlation in the vertical direction corresponding to $\mathbf{B}_{T_{\mathrm{g}},P_{\mathrm{s}},\theta}$ on land and sea. Since there is no T_{g} in the sea, the off-diagonal components of the vertical error correlation matrix associated with T_{g} are zero. Both on land and sea, P_{s} is negatively correlated with θ. Characteristically, in the lower atmosphere (e.g., the model levels from 1 to 5), the error correlation distance of θ in the vertical direction on land is larger than that on sea. The variance of pseudo relative humidity (RH) is smaller on the land grid point than on the sea grid point (e.g., Fig. 1d). The few layers near the model top are damping layers to merge the parent model, and then, the growth of forecast error in those layers is suppressed. Consequently, the background error covariance around the model top reaches zero. Figure 3 shows the horizontal autocorrelation length of background error for each analysis element calculated by the lagged NMC method. The horizontal autocorrelation lengths are taken to be different in the x and y directions but are not classified by land, sea, or local time. One of the reasons we did not classify the horizontal autocorrelations in local time was that it did not improve the forecast accuracy.

Fig. 1

Fig. 2

Fig. 3

2.4 Observation term

The observation term measures the distance between the observation and the model state. To compare the observation and the model, the NWP model is integrated to the observation time using the model operator and the observation is simulated using the observation operator. This section details the model operator and the observation operator.

a. Model operator

The 4D-Var method iteratively runs the time integration of the NWP model during variational optimization, accounting for most of the computational cost. To reduce the calculation cost, an incremental method with the basic field updates (see subsection 2.1b) is used, and it also runs the time integration at low resolution. In the incremental method, the first guess is calculated with a high-resolution model to obtain the misfit with observation. Conversely, a low-resolution model is used in the iteration of the optimization calculation for minimizing the cost function.

ASUCA-Var uses the JMA non-hydrostatic model ASUCA as its nonlinear model operator. Table 1 shows the ASUCA configuration as model operator for high and low resolution. The low-resolution model variants are classified as nonlinear (NL), tangent-linear (TL) which is a tangent form of the NL, and adjoint (AD) which is the transpose of the TL. Table 1

The high-resolution model is the same as the MSM. The grid spacing of the high-resolution model is 5 km, and the number of vertical layers is 76. The model's top height is approximately 22 km. The ground temperature is divided into eight layers, and soil volumetric water content is divided into two layers. The prognostic variables are: ρ (kg m^{-3}) is air density; ρu, ρv, and ρw (kg m^{-2} s^{-1}) are the flux forms of (u, v, and w) wind components in Cartesian coordinates, respectively; $\rho\theta_{\mathrm{m}}$ (kg m^{-3} K) is the flux form of virtual moist potential temperature; ρq_{α} $(\alpha = \mathrm{v, c, r, i, s, g})$ (kg m^{-3} kg kg^{-1}) is the flux form of water vapor and hydrometeors; T_{g} is the soil temperature; and W_{g} is the soil volumetric water content.

The NL model is basically the same as the high-resolution model except for its low resolution and the convective parameterization. The horizontal grid spacing of the low-resolution model is 15 km, and the number of vertical layers is 38. The height of the model top is the same as that of the high-resolution model. The parameters of physics schemes (e.g., convective parameterization), which depend on the grid spacing, are modified to be suited for the 15 km grid spacing of the NL model.

The grid spacing and the number of layers in the TL model are the same as in the NL. The dynamics in the TL model are linearized without simplifying the dynamics of the NL model. The physics schemes of the TL model are simplified to avoid severe linear approximation errors due to the strong nonlinearity of the NL model. Table 1 shows a summary of each scheme. The boundary layer scheme has a fixed diffusion coefficient of the background field. The surface process fixes the background bulk coefficients. Radiation has a very simple implementation based on Mahfouf (1999). The cloud microphysics process converts water vapor perturbations into precipitation perturbations through tangent-linearized saturation adjustment. Other elementary processes of cloud microphysics and convective parameterization are not linearized, and those perturbations are ignored.

Figure 4 shows the comparison between NL perturbation, $\mathcal{M}_{i,0}\left(\mathbf{x}_0^{\mathrm{g}} + \delta\mathbf{x}_0\right) - \mathcal{M}_{i,0}\left(\mathbf{x}_0^{\mathrm{g}}\right)$, and TL perturbation, $\mathbf{M}_{i,0}\delta\mathbf{x}_0$, in the initial condition of MSM at 0000 UTC 7 July 2018. Figure 4a shows the integrated q_{v} in the vertical direction in the background field. To compare the NL and the TL perturbations, the pseudo initial perturbation of q_{v} is set at the 10-th layer. The shape of the initial perturbation is Gaussian with the standard deviation of 7-grid/3-layer in horizontal/vertical direction, and the horizontal distribution of it is shown in Fig. 4b. There is no significant difference between the NL and TL perturbations of the water vapor field after the time integration of 3 hours in the assimilation window [T−3h,T+0h] (Figs. 4c-d). However, the TL perturbations of precipitation are smaller than the NL perturbations, and in particular, the TL cannot predict well convective precipitation over the southern region of Japan (Figs. 4e-f). This difference in predicted perturbation is caused by the limitation of TL with simplified physical processes. This result also implies the necessity of the basic field update by NL.

Fig. 4

The AD model is described by a code that is an exact transposition of the TL model code. The accuracy of the transposed code is required to satisfy the verification equation in a double-precision system as

$$\|\mathbf{M}_{n,0}\delta\mathbf{x}_0\|_2^2 - \delta\mathbf{x}_0^{\mathrm{T}}\left(\mathbf{M}_{n,0}^{\mathrm{T}}\mathbf{M}_{n,0}\delta\mathbf{x}_0\right) = \mathcal{O}\left(10^{-15}\right), \tag{29}$$

where the assimilation window t_n is 3 h.

Table 2

b. Observation operator

The observation operator computes the model version of the observation, which is projected from the model state into the observation space. Table 2 shows the acronyms related to observations. Wind speed, temperature, and

RH, as observed by radiosonde and SYNOP, are provided with spatial interpolation and diagnostic processes, transforming the model variables into observed variables. RH is given in the guide (World Meteorological Organization, 2017, PART I Chapter 4), and is calculated as

$$\begin{aligned} RH &= \frac{p r_{\mathrm{v}}}{\left(\varepsilon + r_{\mathrm{v}}\right) e_{\mathrm{sat}}} &(30)\\ &= \frac{p q_{\mathrm{v}}}{\left(\varepsilon + \left(1-\varepsilon\right) q_{\mathrm{v}}\right) e_{\mathrm{sat}}}, &(31)\end{aligned}$$

$$\varepsilon = \frac{R_{\mathrm{d}}}{R_{\mathrm{v}}}, \tag{32}$$

where p (Pa) is the hydrostatic pressure, q_{v} is the specific humidity, $r_{\mathrm{v}}(= q_{\mathrm{v}}(1-q_{\mathrm{v}})^{-1})$ is the mixing ratio, R_{d} (= 287.05 J kg^{-1} K^{-1}) is the gas constant for dry air, R_{v} (= 461.5 J kg^{-1} K^{-1}) is the gas constant for water vapor, and e_{sat} (Pa) is the water-saturated water vapor pressure from Tetens formula (Tetens, 1930).

Surface observations (e.g., SYNOP, AMeDAS, and ASCAT) are assimilated using the observation operator based on the surface flux scheme (Beljaars and Holtslag, 1991). Wind speed at 10 m altitude is given as

$$u_{10\mathrm{m}} = \sqrt{\frac{C_{\mathrm{m}}\left(z_1\right)}{C_{\mathrm{m}}\left(z_{10\mathrm{m}}\right)}} u_1, \tag{33}$$

where z_1 and u_1 are the altitude and wind speed at the bottom layer of the model's atmosphere, $z_{10\mathrm{m}}$ and $u_{10\mathrm{m}}$ are the altitude and wind speed at 10 m from the surface, and $C_{\mathrm{m}}(\cdot)$ is the momentum bulk coefficient (Beljaars and Holtslag, 1991).

The temperature at 1.5 m is calculated from the potential temperature at 1.5 m and the surface pressure. The potential temperature and specific humidity at 1.5 m are given as

$$\theta_{1.5\mathrm{m}} = \theta_{\mathrm{s}} + \frac{C_{\mathrm{h}}\left(z_1\right)}{C_{\mathrm{h}}\left(z_{1.5\mathrm{m}}\right)}\sqrt{\frac{C_{\mathrm{m}}\left(z_1\right)}{C_{\mathrm{m}}\left(z_{1.5\mathrm{m}}\right)}}\left(\theta_1 - \theta_{\mathrm{s}}\right), \tag{34}$$

$$\theta_{\mathrm{s}} = \frac{T_{\mathrm{g,skin}}}{\pi_{\mathrm{s}}}, \tag{35}$$

$$q_{\mathrm{v}1.5\mathrm{m}} = q_{\mathrm{vs}} + \frac{C_{\mathrm{q}}\left(z_1\right)}{C_{\mathrm{q}}\left(z_{1.5\mathrm{m}}\right)}\sqrt{\frac{C_{\mathrm{m}}\left(z_1\right)}{C_{\mathrm{m}}\left(z_{1.5\mathrm{m}}\right)}}\left(q_{\mathrm{v}1} - q_{\mathrm{vs}}\right), \tag{36}$$

$$q_{\mathrm{vs}} = (1-\beta)q_{\mathrm{sat,s}} + \beta q_{\mathrm{v}1}, \tag{37}$$

$$\beta = \begin{cases} W_{\mathrm{g}}/0.3 & W_{\mathrm{g}} \leq 0.3 \\ 1 & W_{\mathrm{g}} > 0.3 \end{cases}, \tag{38}$$

where θ_1 and $q_{\mathrm{v}1}$ are the potential temperature and specific humidity at the bottom layer of the model's atmosphere. θ_{s}, $T_{\mathrm{g,skin}}$, π_{s}, q_{vs}, $q_{\mathrm{sat,s}}$, β, and W_{g} are the potential temperature, ground temperature, Exner function, specific humidity, saturated specific humidity, evaporation rate, and volumetric soil moisture content at the model's skin layer. $C_{\mathrm{h}}(\cdot)$ and $C_{\mathrm{q}}(\cdot)$ are the heating and latent heating bulk coefficient (Beljaars and Holtslag, 1991). The surface grid for calculating the meteorological elements of the earth's surface has land tiles and sea tiles. The surface flux F depends on the type of those surfaces and is given by

$$F = (1 - C_{\mathrm{sea}})F_{\mathrm{land}} + C_{\mathrm{sea}}F_{\mathrm{sea}}, \tag{39}$$

where $C_{\rm sea}$ is the covered rate of sea and $F_{\rm land}$ ($F_{\rm sea}$) is surface flux from the land (sea) in the inner model. The effects from surface observations along the coastline are weighted by $C_{\rm sea}$ in the adjoint operator.

Doppler velocities observed by Doppler radar are simulated by only the horizontal wind component of air. As shown in Ishikawa and Koizumi (2006), only low elevation scans below 5.9° are used for assimilation, so the contributions of hydrometeors and vertical velocity of air to Doppler velocities are ignored for simplification. The Doppler velocity V_r (m s^{-1}) at altitude z (m) is

$$V_r\left(z\right) = \frac{\sum_{k=1}^{n_z}\left(u_k \sin\theta + v_k \cos\theta\right) \exp\left[-\left(\frac{z_k - z}{d\delta\phi}\right)^2\right]}{\sum_{k=1}^{n_z} \exp\left[-\left(\frac{z_k - z}{d\delta\phi}\right)^2\right]}, \tag{40}$$

where u_k, v_k, and z_k are the x direction wind component, y direction wind component, and altitude at the model's k-th layer; n_z is the number of model layers; d (m) is the distance from the radar site, and $\delta\phi\,(= 0.3°)$ is the beam width of the antenna pattern. Additionally, radar reflectivity is assimilated as RH derived from it using the One-dimensional Maximum Likelihood Estimation (1D-MLE)+4D-Var method (Ikuta and Honda, 2011; Ikuta et al., 2021).

Model precipitable water vapor (PWV) is obtained by integrating the mass of water vapor from the surface to the top model layer $z_{\rm top}$ as follows:

$$PWV[\text{mm}] = \int_0^{z_{\rm top}} \rho q_{\rm v} dz, \tag{41}$$

where ρ is air density. Ground-based GNSS observations widely deployed in Japan have been assimilated for PWV (Ishikawa, 2010).

The Radar/Raingauge-Analyzed Precipitation (R/A: Nagata, 2011) and precipitation retrievals from satellite data are assimilated as the amount of 1 h accumulation in MA. Only precipitation observations above 0.5 mm h^{-1} are used, and no-precipitation information is not used. The observation error and the probability density function (PDF) for precipitation observations are defined as in Koizumi et al. (2005), and the observation term for precipitation in the cost function is approximated in quadratic form as

$$J^{\mathrm{prc}} = -\frac{1}{2}\left(\frac{\hat{y}_{\mathrm{prc}} - \hat{y}^{\mathrm{o}}_{\mathrm{prc}}}{r}\right)^2, \tag{42}$$

$$r = \begin{cases} r_{\mathrm{inf}} \max\left(\hat{y}^{\mathrm{o}}_{\mathrm{prc}}, 1\right) & \left(\hat{y}_{\mathrm{prc}} \leq \hat{y}^{\mathrm{o}}_{\mathrm{prc}}\right) \\ r_{\mathrm{inf}} r_{\mathrm{asy}} \max\left(\hat{y}^{\mathrm{o}}_{\mathrm{prc}}, 1\right) & \left(\hat{y}_{\mathrm{prc}} > \hat{y}^{\mathrm{o}}_{\mathrm{prc}}\right) \end{cases}. \tag{43}$$

The R/A assimilation is used with the inflation factor $r_{\mathrm{inf}} = 1$ and the asymmetricity factor $r_{\mathrm{asy}} = 3$. The precipitation retrievals from satellite data is assimilated with $r_{\mathrm{inf}} = 2$ and $r_{\mathrm{asy}} = 5$. $\hat{y}_{\mathrm{prc}}$ and $\hat{y}^{\mathrm{o}}_{\mathrm{prc}}$ are variables modified from the 1 h accumulated precipitation from the forecast y_{prc} (mm h^{-1}) and observed $y^{\mathrm{o}}_{\mathrm{prc}}$ (mm h^{-1}) as described below. Originally, this formulation was applied to the original precipitation values y_{prc} and $y^{\mathrm{o}}_{\mathrm{prc}}$, but it was very sensitive to rain intensity and PDF of the observation error remained non-Gaussian, which negatively affected the accuracy of the predictions. Therefore, y_{prc} was converted to the new variable $\hat{y}_{\mathrm{prc}}$ in a manner similar to the Box–Cox transformation (Box and Cox, 1964) method:

$$\hat{y}_{\mathrm{prc}} = \begin{cases} \frac{y_{\mathrm{prc}}^{\lambda}-1}{\lambda}+1 & (y_{\mathrm{prc}} > 1) \\ y_{\mathrm{prc}} & (y_{\mathrm{prc}} \leq 1) \end{cases}, \tag{44}$$

where $\lambda = 1/3$. This parameter was determined through trial and error to improve the forecast accuracy. $\hat{y}^{\mathrm{o}}_{\mathrm{prc}}$ is calculated from $y^{\mathrm{o}}_{\mathrm{prc}}$ in the same way as $\hat{y}_{\mathrm{prc}}$.

Brightness temperatures of satellite observations are simulated using RTTOV (Radiative Transfer for TOVS: Saunders et al., 2018) and have been assimilated as clear sky radiance (Kazumori, 2014; Ikuta, 2017a). Refractivity is simulated from GNSS radio occultation measurements by ROPP (Radio Occultation Processing Package: ROM SAF, 2019) and has been assimilated in MA (Hirahara et al., 2017). These external simulators are integrated in a common interface of ASUCA-Var's observation operators. By packaging the external simulators in this way, their version dependence in the DA core is reduced and development efficiency is improved.

c. Variational quality control

Some observations are subject to variational quality control (VarQC: Anderson and Järvinen, 1999). In MA, the VarQC covers radiosonde, wind profiler (WPR), and aircraft observations (Yoshimoto, 2010). A VarQC PDF is defined as a mixture of normally distributed (N) and uniformly distributed (F) PDFs as follows. F derived from gross error is given by

$$F = \frac{1}{2d\sigma_{\mathrm{o}}}, \tag{45}$$

where σ_{o} is the standard deviation of a single observation error that is the subject of VarQC. $2d\sigma_{\mathrm{o}}$ is a range of possible observation values, and d is a parameter that determines the range. The mixed PDF p^{QC} consisting of N and F is defined as

$$p^{\mathrm{QC}} = (1 - p_{\mathrm{g}})\, N + p_{\mathrm{g}} F, \tag{46}$$

$$N = \frac{1}{\sqrt{2\pi}\sigma_{\mathrm{o}}} e^{-J^{\mathrm{o}}}, \tag{47}$$

where p_{g} is the rate at which gross errors occur and J^{o} is an observation term of the cost function for a single observation. The observation term of the cost function based on p^{QC} is written by

$$J^{\mathrm{QC}} = -\ln p^{\mathrm{QC}} = -\ln \frac{\gamma + e^{-J^{\mathrm{o}}}}{\gamma + 1}, \tag{48}$$

$$\gamma = \frac{p_{\mathrm{g}}\sqrt{2\pi}}{(1 - p_{\mathrm{g}})\, 2d}. \tag{49}$$

The gradient of J^{QC} is given as

$$\nabla J^{\mathrm{QC}} = \nabla J^{\mathrm{o}} \cdot \left(1 - \frac{\gamma}{\gamma + e^{-J^{\mathrm{o}}}}\right), \tag{50}$$

where $\left(1 - \frac{\gamma}{\gamma + e^{-J^{\mathrm{o}}}}\right)$ is called VarQC weight. Figure 5 shows J^{o}, J^{QC}, ∇J^{o}, and ∇J^{QC}. For large innovation values, ∇J^{QC} approaches zero, and the observation impact is lost. The observation term for wind observation is described as

$$J_{uv}^{\mathrm{QC}} = -\ln \frac{\gamma_{uv} + e^{-J_u^{\mathrm{o}} - J_v^{\mathrm{o}}}}{\gamma_{uv} + 1}, \tag{51}$$

$$\gamma_{uv} = \frac{\left[1 - \left(1 - p_{u\mathrm{g}}\right)\left(1 - p_{v\mathrm{g}}\right)\right]}{\left(1 - p_{u\mathrm{g}}\right)\left(1 - p_{v\mathrm{g}}\right) 2d_u 2d_v}, \tag{52}$$

where u is the x direction wind velocity, J_u^{o} is an observation term, $p_{u\mathrm{g}}$ is the gross error occurrence rate, and d_u is the coefficient that determines the observable range. Variables with the subscript v, which is y direction wind, are defined in the same way. The allocation of costs shared by u and v is given as

$$J_u^{\mathrm{QC}} = \frac{J_{uv}^{\mathrm{QC}}}{J_u^{\mathrm{o}} + J_v^{\mathrm{o}}} J_u^{\mathrm{o}}, \tag{53}$$

$$J_v^{\mathrm{QC}} = \frac{J_{uv}^{\mathrm{QC}}}{J_u^{\mathrm{o}} + J_v^{\mathrm{o}}} J_v^{\mathrm{o}}. \tag{54}$$

VarQC is enabled from the first iteration in the optimization. Therefore, outliers are invalidated at the first iteration. However, since the current system assimilates a wide variety of observations, the analysis increment is calculated by assimilating observations other than outliers. Then, the cost function is minimized and the basic field is updated. The basic field update changes the VarQC weight in Eq. (50). If the VarQC weight of an observation that was an outlier in the first iteration is increased after the basic field updates, that observation has a chance of recovering to effective observation. Fig. 5

2.5 Variational Bias Correction term

The VarBC method in our system is used to correct for the satellite brightness temperature bias. The brightness temperature bias in the clear sky region is estimated by several predictor variables. The predictors are defined as follows:

- $\mathbf{p}_1$, constant (=1);
- $\mathbf{p}_2$, function of sea surface temperature T_{sst} (K) at scan position;
- $\mathbf{p}_3$, function of satellite angle θ_{sat} (rad);
- $\mathbf{p}_4$, function of orbit flag l_{orbit}.

These predictors are determined with reference to Sato (2007), and the form of the functions are shown below in Eqs. (56)–(58). To simplify the discussion, we consider the case where there is only k-th observation to which VarBC is applied. The bias in this case is given as

$$[\mathcal{P}(\boldsymbol{\beta})]_k = \sum_{i=1}^{N_{\mathrm{p}}} [\mathbf{p}_i]_k [\boldsymbol{\beta}]_{l(k),i}, \tag{55}$$

where $N_{\mathrm{p}} (= 4)$ is the number of predictors and the subscript $l(k)$ indicates the subset to which the k-th observation belongs. Specifically, the subset is grouped by satellite, sensor, and channel. The predictors corresponding to k-th observation are defined as follows:

$$[\mathbf{p}_2]_k = \frac{T_{\mathrm{sst},k} - 273.15}{10.0}, \tag{56}$$

$$[\mathbf{p}_3]_k = 1/\max\left(2\times 10^{-4}, \cos\theta_{\mathrm{sat},k}\right), \tag{57}$$

$$[\mathbf{p}_4]_k = \begin{cases} 1 & l_{\mathrm{orbit},k} = \text{ascending orbit (northwrad)} \\ -1 & l_{\mathrm{orbit},k} = \text{descending orbit (southward)} \end{cases}, \tag{58}$$

where $T_{\mathrm{sst},k}$, $\theta_{\mathrm{sat},k}$, and $l_{\mathrm{orbit},k}$ are the values corresponding to the k-th observation. These predictors can only be derived from observation information and are independent of the forecast model because T_{sst} is fixed in the JMA regional forecast model. Thus, the bias corresponding to the predictors is corrected, even though TL and AD of the predictors are not required in the calculation of the cost function gradient.

The VarBC background error is defined by the method of Cameron and Bell (2018) as follows:

$$B_{\mathrm{bc}} = \frac{\sigma_{\mathrm{o}}^2}{N_{\mathrm{b}}}, \tag{59}$$

$$N_{\mathrm{b}} = \max\left(m_{\mathrm{avg}}, m_{\mathrm{min}}\right) \times \left(\frac{1}{2^{\frac{1}{n}} - 1}\right), \tag{60}$$

$$m_{\mathrm{min}} = 500, \tag{61}$$

where σ_{o} is the observation error, m_{avg} is the average number of observations assimilated during the last 3 days, m_{min} is a lower limit of the number of observations, and n is a parameter that specifies the bias halving time for the convergence of coefficient learning. The halving time parameter of the MA was set as $n = 8$; that of the LA was set as $n = 24$. These halving time parameters were determined based on the number of assimilations per day for each system (Fig. 6). By setting these halving-times, the rapid fluctuation of the coefficients calms down in about 10 days in an experiment that starts with the VarBC coefficients of all satellites as zero. Such insensitivity is necessary to reduce the effects of sudden outliers of observation. We can slow down the response of background error to the presence or absence of observations in the assimilation window by using the average number of observations. This is especially useful for the assimilation of polar-orbiting satellites in a regional model where the forecast domain is limited. In a regional model, a polar-orbiting satellite is only available twice a day; therefore, it is not appropriate to determine B_{bc} depending only on the number of observations assimilated in a single previous analysis. However, by using m_{avg}, we can maintain a history of approximately 3 days to provide a stable bias correction for observations that are less frequently revisited. Fig. 6

The old MA that was in operation until March 25, 2020, did not use VarBC but instead used the VarBC coefficients of the Global DA System (Kazumori, 2014). The commonality of bias correction coefficients between models with completely different resolution and physical processes is not necessarily validated and cannot correct for bias well. For example, Benáček and Mile (2019) demonstrated the effectiveness of VarBC in a regional model by comparing bias correction with VarBC coefficients by global DA and those by the limited-area model DA. At the JMA, the clear sky brightness temperature assimilation and VarBC for the LA were introduced simultaneously (Ikuta, 2017a). In the MA, VarBC was introduced at the same time as the introduction of ASUCA-Var (Ikuta et al., 2020). It is shown in subsection 4.2 that bias correction accuracy is greatly improved by using the MA VarBC.

2.6 Penalty term

The predictions of the NWP model from initial conditions, comprising the first guess plus an increment, will cause high-frequency oscillations due to artificial gravity waves. We implemented a DF method (Lynch, 1997) with a low-pass filter as a constraint to remove these oscillations. In this DF method, noise in the center of the assimilation window is removed by a filter using the Chebyshev window function. DF using the Chebyshev window function has been applied in several 4D-Var systems (e.g., Gustafsson, 1992; Polavarapu et al., 2000; Gauthier and Thépaut, 2001), including the previous MA based on JNoVA (Honda and Sawada, 2010; Sawada and Honda, 2008). The elements to be filtered, based on Wee and Kuo (2004), are the same as those of the background error variance. $\mathbf{B}_{\mathrm{df}}$ in Eq. (7) was given by the diagonal component of the background error $\mathbf{B}_0$ as

$$\mathbf{B}_{\mathrm{df}} = \lambda \mathrm{diag}\left(\mathbf{B}_0\right), \tag{62}$$

where λ is the weighting parameter. The time span for the low-pass filter is described as $T_{\mathrm{s}} = M\Delta t$, with timestep Δt of time integration and M related to the number of total steps as $N = 2M + 1$. The filtered state at $N/2$ is given as

$$\bar{\mathbf{x}}_{\frac{N}{2}} = \sum_{k=0}^{N} \alpha_k \mathbf{x}_k, \tag{63}$$

where α_k is defined as follows:

$$\alpha_k = \frac{h_k w_k}{\sum_{k'=0}^{N} h_{k'} w_{k'}}, \tag{64}$$

$$h_k = \frac{\sin(\theta_{\mathrm{c}} k)}{k\pi}, \tag{65}$$

and the Dolph–Chebyshev window function is given by

$$w_k = \frac{1}{N}\left[1 + 2r\sum_{m=1}^{M} T_{2M}\left(x_0 \cos\frac{\theta_m}{2}\right)\cos m\theta_m\right], \tag{66}$$

where $1/x_0 = \cos(\theta_s/2)$, $1/r = \cosh\left(2M\cosh^{-1} x_0\right)$, $\theta_m = 2\pi m/N$, θ_{c} is the cutoff frequency, θ_s is the stop-band edge, and T_{2M} is the Chebyshev polynomial of degree $2M$:

$$T_{2M}(x) = \begin{cases} \cos\left(2M\cos^{-1} x\right) & |x| \leq 1 \\ \cosh\left(2M\cosh^{-1} x\right) & |x| > 1 \end{cases}. \tag{67}$$

The high-frequency oscillations that will be filtered out are defined as:

$$\mathbf{x}_{\frac{N}{2}} - \bar{\mathbf{x}}_{\frac{N}{2}} = \sum_{k=0}^{N} \gamma_k \mathcal{M}_{k,0}(\mathbf{x}_0), \tag{68}$$

where the coefficient γ_k is given as

$$\gamma_k = \begin{cases} -\alpha_k & k \neq \frac{N}{2} \\ 1 - \alpha_k & k = \frac{N}{2} \end{cases} . \tag{69}$$

In the operational system, the assimilated observations are used under strict quality control. Additionally, the density of the atmosphere at the beginning of the time integration is built based on the hydrostatic assumption. Therefore, noise caused by the large oscillation of artificial gravity waves is considerably suppressed. Particularly, in an ongoing assimilation cycle, the cost of the penalty term is kept small compared with the cost of other terms because ASUCA eliminates the generation of artificial noise as much as possible.

2.7 Preconditioning

a. Control variables

A simplification is applied to the background term by transforming the analysis variables into control variables to solve the optimization problem efficiently. The analysis increment $\delta\mathbf{x}_0$ is described by the analysis variable $\mathbf{x}_0$ and background variable $\mathbf{x}_0^{\mathrm{b}}$ as

$$\delta\mathbf{x}_0 = \mathbf{x}_0 - \mathbf{x}_0^{\mathrm{b}}. \tag{70}$$

The control variable χ is given as

$$\chi = \begin{pmatrix} \chi_0 \\ \chi_{\mathrm{bc}} \end{pmatrix}, \tag{71}$$

$$\begin{pmatrix} \delta \mathbf{x}_0 \\ \delta \boldsymbol{\beta} \end{pmatrix} = \begin{pmatrix} \mathbf{B}_0^{\frac{1}{2}} & 0 \\ 0 & \mathbf{B}_{\mathrm{bc}}^{\frac{1}{2}} \end{pmatrix} \begin{pmatrix} \chi_0 \\ \chi_{\mathrm{bc}} \end{pmatrix}, \tag{72}$$

where $\mathbf{B}_0^{1/2}$ is the square root of the background error covariance matrix and χ_0 is the control variable for the model state. $\mathbf{B}_{\mathrm{bc}}^{1/2}$ and χ_{bc} are the square root of the covariance matrix and the control variable for VarBC. The transformed χ is a dimensionless quantity and each component is uncorrelated. This transformation into control variables is called preconditioning, which makes it unnecessary to calculate the inverse of the background error covariance matrix.

The calculation is further simplified by assuming that vertical and horizontal background errors are independent. We define $\mathbf{B}_0^{1/2}$, decomposed into horizontal and vertical directions, as follows:

$$\mathbf{B}_0^{\frac{1}{2}} = \mathbf{V}\mathbf{C}_{\mathrm{h}}^{\frac{1}{2}}\mathbf{B}_{\mathrm{v}}^{\frac{1}{2}}, \tag{73}$$

where $\mathbf{B}_{\mathrm{v}}^{1/2}$ is the square root of the vertical error covariance matrix, $\mathbf{C}_{\mathrm{h}}^{1/2}$ is the square root of the horizontal error correlation matrix, and $\mathbf{V}$ is a transformation matrix of the vertical coordinate.

$\mathbf{C}_{\mathrm{h}}^{1/2}$ is an isotropic recursive filter (RF) (Purser et al., 2003) that acts as a self-adjoint quasi-Gaussian filter. The RF is applied in the x direction and then in the y direction. Defining the operations in the x direction as $\mathbf{C}_{\mathrm{h}x}^{1/2}$ and the operations in the y direction as $\mathbf{C}_{\mathrm{h}y}^{1/2}$, $\mathbf{C}_{h}^{1/2}$ can be written as

$$\mathbf{C}_{\mathrm{h}}^{\frac{1}{2}} = \mathbf{C}_{\mathrm{h}y}^{\frac{1}{2}}\mathbf{C}_{\mathrm{h}x}^{\frac{1}{2}}. \tag{74}$$

First, we focus on the operations in the x direction. As the same operation is performed in the y direction, we do not describe it. Assuming the correlation distance is horizontally uniform, $\mathbf{C}_{\mathrm{h}x}^{-1/2}$ can be Cholesky decomposed as $\mathbf{C}_{\mathrm{h}x}^{-1/2} = \mathbf{U}^{\mathrm{T}}\mathbf{U}$, and this inverse matrix can be written as

$$\mathbf{C}_{\mathrm{h}x}^{\frac{1}{2}} = \mathbf{U}^{-1}\left(\mathbf{U}^{\mathrm{T}}\right)^{-1}, \tag{75}$$

where $\mathbf{U}$ is an upper triangular matrix. With any input vector $\mathbf{p}$, intermediate vector $\mathbf{q}$, and output vector $\mathbf{s}$, the operations of $\mathbf{U}^{-1}\left(\mathbf{U}^{\mathrm{T}}\right)^{-1}$ can be described by two separate calculations as

$$\mathbf{q} = \left(\mathbf{U}^{\mathrm{T}}\right)^{-1}\mathbf{p}, \tag{76}$$

$$\mathbf{s} = \mathbf{U}^{-1}\mathbf{q}. \tag{77}$$

These equations can be rewritten as

$$q_i = \beta p_i + \sum_{j=1}^{n} \alpha_j q_{i-j}, \tag{78}$$

$$s_i = \beta q_i + \sum_{j=1}^{n} \alpha_j s_{i+j}, \tag{79}$$

where $\beta = 1/U_{i,i}$ and $\alpha_j = -U_{i,i+j}/\beta$. In the recurrence formulas Eqs. (78)-(79), q_i is calculated from p_i in the x direction where i increases and s_i is calculated from q_i in the x direction where i decreases. The order of the RF n is set to 4. For a finite domain RF, boundary conditions need to be set appropriately. The boundary condition in a finite domain $i \in [1, N]$ is given as

$$\left(\hat{\mathbf{L}}^{\mathrm{T}} - \hat{\mathbf{U}}^{\mathrm{T}}\hat{\mathbf{L}}^{-1}\hat{\mathbf{L}}\right)\hat{\mathbf{s}}_N = \beta\hat{\mathbf{q}}_N, \tag{80}$$

where $\hat{\mathbf{L}}$ is a lower triangular $n \times n$ matrix, of which the elements are $\hat{L}_{i,i} = 1$ and $\hat{L}_{i+j,i} = -\alpha_j$; $\hat{\mathbf{U}}$ is an upper triangular $n \times n$ matrix, of which the elements are $\hat{U}_{i,i+j} = -\alpha_{n-j}$. $\hat{\mathbf{s}}_N$ is a sub-vector of $\mathbf{s}$ and defined as $\hat{\mathbf{s}}_N = (s_{N+1-n}, \cdots, s_N)^{\mathrm{T}}$. $\hat{\mathbf{q}}_N$ is a sub-vector of $\mathbf{q}$ in the same way as $\hat{\mathbf{s}}_N$. In the operational system, α_j and β are precomputed assuming twice the number of grids in x and y direction of actual analysis area, and only components in the effective area are extracted and used. This preparation suppresses post-filtering distortion near the boundary. For example, without the preparation for boundary condition of RF, analysis increments near the boundary are excessively suppressed.

The square root of the vertical background error covariance matrix is given as

$$\mathbf{B}_{\mathrm{v}}^{\frac{1}{2}} = \mathbf{U}_{\mathrm{v}}\mathbf{\Lambda}_{\mathrm{v}}^{\frac{1}{2}}\mathbf{U}_{\mathrm{v}}^{\mathrm{T}}, \tag{81}$$

where $\mathbf{\Lambda}_{\mathrm{v}}$ is the diagonal matrix whose elements are the eigenvalues of $\mathbf{B}_{\mathrm{v}}$

and $\mathbf{U}_\mathrm{v}$ is the orthogonal matrix composed of the eigenvectors of $\mathbf{B}_\mathrm{v}$. The model's vertical coordinate is the terrain following coordinate. Conversely, the control variables are located in a vertical coordinate system that is less dependent on terrain. In Eq. (73), $\mathbf{V}$ is the transformation matrix of the vertical coordinate for the control variable to the model's vertical coordinate, as in Fujita (2010) and Fukuda et al. (2011). In ASUCA-Var, $\mathbf{V}$ is defined for each u-, v-, and p-point where the control variables are located. Figure 7 shows the impact of the transformation of the vertical coordinate. By using the transformation, the analysis increments distorted along the terrain are better eliminated than in the case without using it. Fig. 7

b. Parameter transformation

The initial perturbation of the TL model is created by a parameter transformation from the analysis increment $\delta x_0 = (\delta u, \delta v, \delta T_\mathrm{g}, \delta P_\mathrm{s}, \delta\theta, \delta W_\mathrm{g}, \delta\mu_\mathrm{p})^\mathrm{T}$ to a perturbation of the prognostic variables of the NWP model. Conversion to perturbation for the mixing ratio is described from the analysis increment of pseudo RH as

$$\delta q_\mathrm{v} = \frac{\partial q_\mathrm{v}}{\partial \mu_\mathrm{p}} \delta\mu_\mathrm{p} \quad (82)$$

$$= \mathcal{Q}_{\mu_\mathrm{p}} \delta\mu_\mathrm{p}, \quad (83)$$

where $\mathcal{Q}_{\mu_\mathrm{p}}$ is Jacobean. The moist potential temperature θ_m is given as follows:

$$\theta_\mathrm{m} = \theta \times \left(1 + \frac{R_\mathrm{v} - R_\mathrm{d}}{R_\mathrm{d}} q_\mathrm{v} - \sum_i q_i\right), \tag{84}$$

where i indicates the kind of hydrometeors: cloud water, rain, cloud ice, snow, and graupel. The perturbation of θ_m is given as

$$\begin{aligned} \delta\theta_\mathrm{m} &= \frac{\partial \theta_\mathrm{m}}{\partial \theta}\delta\theta + \frac{\partial \theta_\mathrm{m}}{\partial q_\mathrm{v}}\frac{\partial q_\mathrm{v}}{\partial \mu_\mathrm{p}}\delta\mu_\mathrm{p} && (85) \\ &= \mathcal{T}_\theta \delta\theta + \mathcal{T}_{\mu_\mathrm{p}}\delta\mu_\mathrm{p}, && (86) \end{aligned}$$

where the perturbation of the mixing ratio for hydrometeors is ignored because the mixing ratios are not analysis variables. The Exner function π at altitude z (m) is diagnosed from the surface pressure P_s (Pa) at the surface altitude z_s (m) and the moist potential temperature θ_m (K) based on hydrostatic balance, as follows:

$$\pi(z) = \pi(z_\mathrm{s}) - \frac{g}{c_\mathrm{p}} \int_{z_\mathrm{s}}^{z} \theta_\mathrm{m}^{-1} dz, \tag{87}$$

$$\pi(z_\mathrm{s}) = \left(\frac{P_\mathrm{s}}{P_{00}}\right)^{\frac{R_\mathrm{d}}{c_\mathrm{p}}}, \tag{88}$$

where $P_{00} = 100\ 000$ Pa, R_d is the gas constant, c_p $(= 7/2\ R_\mathrm{d})$ is the heat capacity for dry air at constant pressure, and g $(= 9.80665\ \mathrm{m\ s^{-2}})$ is gravity acceleration. Air density is calculated from the Exner function and the moist potential temperature:

$$\rho = \frac{P_{00}\pi^{\frac{c_\mathrm{p}}{R_\mathrm{d}}-1}}{R_\mathrm{d}\theta_\mathrm{m}}. \tag{89}$$

The perturbation of density is given as follows:

$$\begin{aligned}
\delta\rho &= \frac{\partial\rho}{\partial P_{\mathrm{s}}}\delta P_{\mathrm{s}} + \frac{\partial\rho}{\partial\theta_{\mathrm{m}}}\delta\theta_{\mathrm{m}} && (90)\\
&= \frac{\partial\rho}{\partial P_{\mathrm{s}}}\delta P_{\mathrm{s}} + \frac{\partial\rho}{\partial\theta_{\mathrm{m}}}\left(\frac{\partial\theta_{\mathrm{m}}}{\partial\theta}\delta\theta + \frac{\partial\theta_{\mathrm{m}}}{\partial\mu_{\mathrm{p}}}\delta\mu_{\mathrm{p}}\right) && (91)\\
&= \mathcal{D}_{P_{\mathrm{s}}}\delta P_{\mathrm{s}} + \mathcal{D}_{\theta}\delta\theta + \mathcal{D}_{\mu_{\mathrm{p}}}\delta\mu_{\mathrm{p}}. && (92)
\end{aligned}$$

The transformation matrix from analysis variables to prognostic variables is written as

$$\begin{pmatrix} \delta(\rho u) \\ \delta(\rho v) \\ \delta(\rho\theta_{\mathrm{m}}) \\ \delta(\rho q_{\mathrm{v}}) \\ \delta\rho \end{pmatrix} = \begin{pmatrix} \rho & 0 & u\mathcal{D}_{P_{\mathrm{s}}} & u\mathcal{D}_{\theta} & u\mathcal{D}_{\mu_{\mathrm{p}}} \\ 0 & \rho & v\mathcal{D}_{P_{\mathrm{s}}} & v\mathcal{D}_{\theta} & v\mathcal{D}_{\mu_{\mathrm{p}}} \\ 0 & 0 & \theta_{\mathrm{m}}\mathcal{D}_{P_{\mathrm{s}}} & \theta_{\mathrm{m}}\mathcal{D}_{\theta} + \rho\mathcal{T}_{\theta} & \theta_{\mathrm{m}}\mathcal{D}_{\mu_{\mathrm{p}}} + \rho\mathcal{T}_{\mu_{\mathrm{p}}} \\ 0 & 0 & q_{\mathrm{v}}\mathcal{D}_{P_{\mathrm{s}}} & q_{\mathrm{v}}\mathcal{D}_{\theta} & q_{\mathrm{v}}\mathcal{D}_{\mu_{\mathrm{p}}} + \rho\mathcal{Q}_{\mu_{\mathrm{p}}} \\ 0 & 0 & \mathcal{D}_{P_{\mathrm{s}}} & \mathcal{D}_{\theta} & \mathcal{D}_{\mu_{\mathrm{p}}} \end{pmatrix} \begin{pmatrix} \delta u \\ \delta v \\ \delta P_{\mathrm{s}} \\ \delta\theta \\ \delta\mu_{\mathrm{p}} \end{pmatrix}. \tag{93}$$

δT_{g} and δW_{g} are assumed to be uncorrelated with each other and are transfomed by identity matrix $\mathbf{I}$. The flux of a scalar variable that ignores perturbations is written as

$$\delta(\rho q_{\alpha}) = q_{\alpha}\mathcal{D}_{P_{\mathrm{s}}}\delta P_{\mathrm{s}} + q_{\alpha}\mathcal{D}_{\theta}\delta\theta + q_{\alpha}\mathcal{D}_{\mu_{\mathrm{p}}}\delta\mu_{\mathrm{p}}, \tag{94}$$

where α includes the mixing ratios of hydrometeors and turbulent kinetic energy. The left sides of Eqs. (93)-(94) are the initial perturbations of prognostic elements of the TL model.

c. *Perfect quadratic form of the cost function*

The cost function is rewritten in a perfect quadratic form

$$
\begin{aligned}
J &= \frac{1}{2}\|\chi\|_2^2 \\
&\quad + \sum_{i=0}^{n}\frac{1}{2}\left\|\mathbf{R}_i^{-\frac{1}{2}}\left(\tilde{\mathbf{H}}_i^{(j)}\tilde{\mathbf{B}}^{\frac{1}{2}}\chi - \tilde{\mathbf{d}}_i^{(j)}\right)\right\|_2^2 \\
&\quad + \frac{1}{2}\left\|\mathbf{B}_{\mathrm{df}}^{-\frac{1}{2}}\left(\tilde{\mathbf{\Gamma}}^{(j)}\tilde{\mathbf{B}}^{\frac{1}{2}}\chi - \tilde{\mathbf{g}}^{(j)}\right)\right\|_2^2, \qquad (95)
\end{aligned}
$$

where

$$\tilde{\mathbf{B}}^{\frac{1}{2}} = \begin{pmatrix} \mathbf{B}_0^{\frac{1}{2}} & 0 \\ 0 & \mathbf{B}_{\mathrm{bc}}^{\frac{1}{2}} \end{pmatrix}, \qquad (96)$$

$$\tilde{\mathbf{H}}_i^{(j)} = \begin{pmatrix} \mathbf{H}_i^{(j)}\mathbf{M}_{i,0}^{(j)} & 0 \\ 0 & \mathbf{P}^{(j)} \end{pmatrix}, \qquad (97)$$

$$\tilde{\mathbf{\Gamma}}^{(j)} = \begin{pmatrix} \mathbf{\Gamma}^{(j)} & 0 \\ 0 & 0 \end{pmatrix}. \qquad (98)$$

The modified innovation of observation $\tilde{\mathbf{d}}_i^{(j)}$ is given as

$$\tilde{\mathbf{d}}_i^{(j)} = \mathbf{d}_i^{(j)} - \mathbf{R}_i^{-\frac{1}{2}}\mathbf{H}_i^{(j)}\mathbf{M}_i^{(j)}\delta\mathbf{x}_0^{\mathrm{b}(j)} - \mathbf{R}_i^{-\frac{1}{2}}\mathbf{P}^{(j)}\delta\boldsymbol{\beta}^{\mathrm{b}(j)}. \qquad (99)$$

The modified innovation of DF $\tilde{\mathbf{g}}^{(j)}$ is given as

$$\tilde{\mathbf{g}}^{(j)} = \mathbf{g}^{(j)} - \mathbf{\Gamma}^{(j)}\delta\mathbf{x}_0^{\mathrm{b}(j)}. \qquad (100)$$

The gradient of the cost function is given as

$$\frac{\partial J}{\partial \chi} = \chi \qquad (101)$$

$$+\sum_{i=0}^{n}\left(\tilde{\mathbf{B}}^{\frac{1}{2}}\right)^{\mathrm{T}}\left(\tilde{\mathbf{H}}_i^{(j)}\right)^{\mathrm{T}}\mathbf{R}_i^{-1}\left(\tilde{\mathbf{H}}_i^{(j)}\tilde{\mathbf{B}}^{\frac{1}{2}}\chi-\tilde{\mathbf{d}}_i^{(j)}\right) \tag{102}$$

$$+\left(\tilde{\mathbf{B}}^{\frac{1}{2}}\right)^{\mathrm{T}}\left(\tilde{\boldsymbol{\Gamma}}^{(j)}\right)^{\mathrm{T}}\mathbf{B}_{\mathrm{df}}^{-1}\left(\tilde{\mathbf{H}}_i^{(j)}\tilde{\mathbf{B}}^{\frac{1}{2}}\chi-\tilde{\mathbf{d}}_i^{(j)}\right). \tag{103}$$

The optimized control variable χ^{a} is given as

$$\chi^{\mathrm{a}}=\min_{\chi} J\left(\chi\right). \tag{104}$$

This minimization problem is solved using the limited-memory Broyden–Fletcher–Goldfarb–Shanno (L-BFGS) quasi-Newton minimization method algorithm (Nocedal, 1980; Liu and Nocedal, 1989). χ^{a} is converted into the analysis variables $\mathbf{x}_0^{\mathrm{a}}$ and $\boldsymbol{\beta}^{\mathrm{a}}$ at the start time of the assimilation window:

$$\mathbf{x}_0^{\mathrm{a}}=\mathbf{x}_0^{\mathrm{b}}+\mathbf{B}_0^{\frac{1}{2}}\chi_0^{\mathrm{a}}, \tag{105}$$

$$\boldsymbol{\beta}^{\mathrm{a}}=\boldsymbol{\beta}^{\mathrm{b}}+\mathbf{B}_{\mathrm{bc}}^{\frac{1}{2}}\chi_{\mathrm{bc}}^{\mathrm{a}}. \tag{106}$$

In MA, the assimilation window is three hours; thus, the model creates an initial condition of the forecast model at analysis time t_n:

$$\mathbf{x}^{\mathrm{a}}\left(t_n\right)=\mathcal{M}_{n,0}\left(\mathbf{x}_0^{\mathrm{a}}\right). \tag{107}$$

2.8 Coding design

One of the issues in developing and continuing to operate 4D-Var is that the model operators used in the forecast model and assimilation will deviate as development progresses. To prevent this, NL,TL, and AD coexist in one subroutine for the purpose of sustainable development. The switching of NL,TL, and AD modes is specified by an input parameter and branched by an if statement. The subroutine arguments and return values are shared by NL,TL, and AD modes. This rule will force a change in TL and AD if NL is changed. That is, the dynamics subroutines, physics library, and observation operator libraries contain NL,TL, and AD code for assimilation.

Figure 8 shows the structure of ASUCA-Var, which comprises an assimilation core to perform optimization and preconditioning, ASUCA as NWP model to perform time integration, a physics library to compute physical processes, and observation operators to simulate observations. All observation operators are archived in the observation operator library. The observation operators included in the library are used via the ASUCA-Var common interface. When implementing an observation operator library developed by other developers, the common interface facilitates new implementations and updates and minimizes changes to existing code. In the operational system, RTTOV and ROPP have been implemented. Fig. 8

2.9 Parallelization

The data assimilation system is envisioned to run in a hybrid environment of message passing interface (MPI) and open multiprocessing (OpenMP). The data assimilation region is decomposed into blocks in two dimensions, each of which is processed by a different MPI process. In the following, the two-dimensional decomposed region is called a block. Observations are also arranged and processed in parallel for each of those blocks. The spatial-horizontal do-loops in that block are forked via OpenMP parallelization.

The RF method used in preconditioning is also parallelized in each block. The calculation of RF in the x direction must be sequential but independent in the y direction, so it is parallelized in the y direction. The RF in the y direction is similarly parallelized in the x direction.

In the adjoint codes for advection and the pressure tendency equation, conflicts occur when applying spatial-horizontal OpenMP parallelization without any special treatment because the adjoint variables are added to the neighboring grid points of the target grid point. To avoid this conflict, the adjoint code is parallelized by the multi-color successive over-relaxation (SOR) method (Adams and Ortega, 1982). The Red-Black SOR method is used when adding to one adjacent grid point. When adding to the adjacent five grid points (or nine grid points), parallelization was performed by the five-color (nine-color) SOR method. The adjoint equations, which require the use of Red-Black, five-color, and nine-color SOR methods, are given as

$$\text{Red-Black}: \quad q_{i,j} = q_{i,j} + q_{i+1,j}, \tag{108}$$

$$\text{5-color}: \quad q_{i,j} = q_{i,j} + q_{i-1,j} + q_{i+1,j} + q_{i,j-1} + q_{i,j+1}, \tag{109}$$

$$\text{9-color}: \qquad q_{i,j} = \sum_{k=i-1}^{i+1} \sum_{l=j-1}^{j+1} q_{k,l}, \tag{110}$$

$$\tag{111}$$

where $q_{i,j}$ represents an arbitrary variable and the subscripts i and j denote the grid numbers. The optimization algorithm is also parallelized. In the computation of cost function minimization, computational efficiency is improved by calculating the inner product of the general vector, which is the input of the L-BFGS, in each block.

3. Operational system

The JMA operates MA and LA as regional data assimilation systems with ASUCA-Var as core method for DA. The MA creates the initial conditions for MSM and the LA creates the initial conditions for LFM. Figure 9 shows the domains of MSM and LFM. These domains cover Japan and its surroundings. In this section, we provide an overview of MA and LA. Fig. 9

3.1 Meso-scale analysis

Figure 10 shows the flow diagram for MA. The formulation of the variational method in MA is described in Section 2. The data assimilation method employs an incremental 4D-Var method, and the iterative optimization with three inner loops (20, 15, and 15 iterations) is conducted, and the basic field is updated twice by the inner model at the connection point of the inner loops. The high-resolution outer model is the same as the MSM. The low-resolution inner model has 15 km horizontal grid spacing, 38 vertical layers, and the same model top as in MSM. The assimilation window starts 3 h before the initial time, and the observation timeslots are set to hourly. The MSM initial conditions are created at 00, 03, 06, 09, 12, 15, 18, and 21 UTC daily, and data assimilation is run eight times a day. In the following, we describe the steps to run the MA. Fig. 10

a. Procedure

STEP 1. The first guess is provided by the 3 h forecast of MSM from the result of the previous MA.

STEP 2. Innovation is calculated with the MSM and observations.

STEP 3. The basic field is calculated with the NL model.

STEP 4. Perturbation is calculated with the TL model (skipped in the first iteration), and the cost function is evaluated.

STEP 5. Gradient of cost is calculated with the AD model.

STEP 6. Analysis increment is calculated by minimization of the cost function using the L-BFGS algorithm.

STEP 7. As the inner loop, steps 4–6 are repeated. The number of inner loop iterations is 20 times in the first outer loop and 15 times in the second and third outer loop.

Finally, the low-resolution analysis from the result of STEP 7 is interpolated to the high resolution of 5 km with consideration of ancillaries (topography, soil type, and land use). From the interpolated analysis, MSM as high-resolution model operator is run from T−3h to T+0h (Fig. 10). The result of the computation becomes the initial condition for the forecast of MSM.

b. Observation

The cutoff time for waiting to receive observation data is 50 min. The assimilated observations in MA are listed as follows (Japan Meteorological Agency, 2019): SYNOP; SHIP; BUOY; TEMP; PILOT; WPR; Weather Doppler radar (radial velocity, reflectivity); AIREP; AMDAR; AMVs from Himawari-8; ocean surface wind from Metop-[A, B]/ASCAT; radiances from NOAA-[15, 18, 19]/ATOVS, Metop-[A, B]/ATOVS, Aqua/AMSU-A, DMSP-F[17, 18]/SSMIS, GCOM-W/AMSR2, and GPM-core/GMI; water vapor CSR from Himawari-8; R/A; precipitation retrievals from DMSP-F[17, 18]/SS-MIS, GCOM-W/AMSR2, and GPM-core/GMI; GPM-core/DPR; GNSS-RO refractivity data from Metop-[A, B]/GRAS, COSMIC/IGOR, GRACE-[A, B]/Blackjack, TerraSAR-X/IGOR, and TanDEM-X/IGOR; and PWV from ground-based GNSS (see Table 2).

3.2 Local analysis

In the LA, the computational time available for data assimilation is very limited because the analysis for the initial condition of LFM is created every hour. As described below, the LA does not cycle itself because the LA's first guess is given by the forecast of MSM. To reduce the computation cost, 3D-Var is used as the data assimilation method for the LA. Because no model operators are used in 3D-Var, basic field updates and DF are not used. Also, VarQC is not used, and the background error is not dependent on the initial time. The cost function is defined as

$$J = J^{\mathrm{b}} + J^{\mathrm{o}} + J^{\mathrm{bc}}. \tag{112}$$

The assimilation window is 3 h before the initial time of LFM, and the observations are assimilated by 3D-Var every hour starting at the initial time of the assimilation window. To calculate the time propagation of analysis increments within the assimilation window, LA repeats the 3D-Var and the 1 h forecast. Figure 11 illustrates the process flow of LA. In the following sections, we show the steps to run the LA. Fig. 11

a. Procedure

There are four timeslots to assimilate observation, at hourly intervals. The analysis $\mathbf{x}^{\mathrm{a}}$ at the initial time of LFM is calculated by repeating 3D-Var and 1 h forecasting. The 1 h forecast operator $\mathcal{M}_{i+1,i}$ from the i-th timeslot to $(i+1)$-th timeslot is configured specifically for the LA. In this configuration, horizontal resolution is set to 5 km as in the MSM, but the physics schemes differ from those used in the MSM. The cycles of LA are performed in the order shown below.

STEP 1. In the first timeslot, the first guess of the model state $\mathbf{x}^{\mathrm{b}}_{i=1}$ is provided by the MSM, and the VarBC coefficient $\boldsymbol{\beta}^{\mathrm{b}}_{i=1}$ inherits the results of the previously run LA.

STEP 2. In the i-th timeslot, the optimized model state $\mathbf{x}^{\mathrm{a}}_i$ and the optimized VarBC coefficients $\boldsymbol{\beta}^{\mathrm{a}}_i$ are defined as

$$\mathbf{x}^{\mathrm{a}}_i = \mathbf{x}^{\mathrm{b}}_i + \delta\mathbf{x}_i, \tag{113}$$

$$\boldsymbol{\beta}^{\mathrm{a}}_i = \boldsymbol{\beta}^{\mathrm{b}}_i + \delta\boldsymbol{\beta}_i, \tag{114}$$

where $\delta\mathbf{x}_i$ and $\delta\boldsymbol{\beta}_i$ are the analysis increments by 3D-Var.

STEP 3. The $(i+1)$-th background state is given by the 1 h integration by $\mathcal{M}_{i+1,i}$:

$$\mathbf{x}^{\mathrm{b}}_{i+1} = \mathcal{M}_{i+1,i}\left(\mathbf{x}^{\mathrm{a}}_i\right), \tag{115}$$

and the background VarBC coefficient inherits the i-th analysis of VarBC as $\boldsymbol{\beta}^{\mathrm{b}}_{i+1} = \boldsymbol{\beta}^{\mathrm{a}}_{i}$.

STEP 4. Steps 2 and 3 are repeated three times.

STEP 5. In the fourth timeslot at the initial time of LFM, the analysis increments by 3D-Var are added to the background states. The analysis values are given as

$$\mathbf{x}^{\mathrm{a}} = \mathbf{x}^{\mathrm{b}}_{4} + \delta\mathbf{x}_{4}, \tag{116}$$

$$\boldsymbol{\beta}^{\mathrm{a}} = \boldsymbol{\beta}^{\mathrm{b}}_{4} + \delta\boldsymbol{\beta}_{4}. \tag{117}$$

Finally, the analysis $\mathbf{x}^{\mathrm{a}}$ with 5 km resolution is interpolated to the 2 km resolution grid with consideration of ancillaries (topography, soil type, and land use) to be used as initial conditions with the LFM. Note that the first guess of the LA is always given and refreshed by the MSM. The results of the LA are not carried over to the next cycle of LA, except for the VarBC coefficients.

b. Observation

The cutoff time for waiting to receive observation data is 30 min. The assimilated observations for the LA are listed as follows (Japan Meteorological Agency, 2019): SYNOP; SHIP; BUOY; AMeDAS; TEMP; PILOT; WPR; Weather Doppler radar (radial velocity, reflectivity); AIREP; AM-

DAR; AMVs from Himawari-8; radiances from NOAA-[15, 18, 19]/ATOVS, Metop-[A, B]/ATOVS, Aqua/AMSU-A, DMSP-F[17, 18]/SSMIS, GCOM-W/AMSR2, and GPM-core/GMI; water vapor CSR from Himawari-8; soil moisture from GCOM-W/AMSR2 and Metop-[A, B]/ASCAT; and PWV from ground-based GNSS (see Table 2).

4. Performance

4.1 Degrees of freedom for signal

Using degrees of freedom for signal (DFS: Cardinali et al., 2004) based on Chapnik et al. (2006), we show the impact of assimilated observations on MA. The DFS, divided into subsets for each observation type, is defined as

$$DFS_k = \mathrm{Tr}\left(\mathbf{\Pi}_k^{\mathrm{o}} \frac{\partial \mathcal{H}\left(\mathbf{x}^{\mathrm{a}}\right)}{\partial \mathbf{y}^{\mathrm{o}}} \mathbf{\Pi}_k^{\mathrm{o}\,\mathrm{T}}\right), \tag{118}$$

where $\mathbf{\Pi}_k^{\mathrm{o}}$ is a projection operator onto the k-th subset. The actual calculation method is as follows. First, the perturbation of the observation vector with vector length p using the random vector $\zeta \sim N\left(0, \mathbf{I}_p\right)$ is given as

$$\delta \mathbf{y}^{\mathrm{o}} = \mathbf{R}^{\frac{1}{2}} \zeta. \tag{119}$$

In practice, using this observed perturbation, DFS is calculated as follows:

$$\left\langle \left(\mathbf{\Pi}_k^{\mathrm{o}} \delta \mathbf{y}^{\mathrm{o}}\right)^{\mathrm{T}} \mathbf{R}_k^{-1} \mathbf{\Pi}_k^{\mathrm{o}} \left\{\mathcal{H}\left[\mathbf{x}^{\mathrm{a}}\left(\mathbf{y}^{\mathrm{o}} + \delta \mathbf{y}^{\mathrm{o}}\right)\right] - \mathcal{H}\left[\mathbf{x}^{\mathrm{a}}\left(\mathbf{y}^{\mathrm{o}}\right)\right]\right\} \right\rangle$$

$$
\begin{aligned}
&= \left\langle \delta \mathbf{y}^{\mathrm{o}\,\mathrm{T}} \boldsymbol{\Pi}_k^{\mathrm{o}\,\mathrm{T}} \mathbf{R}_k^{-1} \boldsymbol{\Pi}_k^{\mathrm{o}} \frac{\partial \mathcal{H}\left(\mathbf{x}^{\mathrm{a}}\right)}{\partial \mathbf{y}^{\mathrm{o}}} \delta \mathbf{y}^{\mathrm{o}} \right\rangle && (120) \\
&= \left\langle \mathrm{Tr}\left[\delta \mathbf{y}^{\mathrm{o}} \delta \mathbf{y}^{\mathrm{o}\,\mathrm{T}} \boldsymbol{\Pi}_k^{\mathrm{o}\,\mathrm{T}} \mathbf{R}_k^{-1} \boldsymbol{\Pi}_k^{\mathrm{o}} \frac{\partial \mathcal{H}\left(\mathbf{x}^{\mathrm{a}}\right)}{\partial \mathbf{y}^{\mathrm{o}}} \right] \right\rangle && (121) \\
&\simeq \mathrm{Tr}\left[\mathbf{R} \boldsymbol{\Pi}_k^{\mathrm{o}\,\mathrm{T}} \mathbf{R}_k^{-1} \boldsymbol{\Pi}_k^{\mathrm{o}} \frac{\partial \mathcal{H}\left(\mathbf{x}^{\mathrm{a}}\right)}{\partial \mathbf{y}^{\mathrm{o}}} \right] && (122) \\
&= \mathrm{Tr}\left[\boldsymbol{\Pi}_k^{\mathrm{o}} \frac{\partial \mathcal{H}\left(\mathbf{x}^{\mathrm{a}}\right)}{\partial \mathbf{y}^{\mathrm{o}}} \boldsymbol{\Pi}_k^{\mathrm{o}\,\mathrm{T}} \right], && (123)
\end{aligned}
$$

where subscript k indicates the subset for each observation type. Figure 12a shows the DFS by observation type. The statistical period is from 0000 UTC 13 June 2018 to 2100 UTC 23 July 2018. We can see that the Doppler velocity and Rain observations have a significant impact. Among the satellite observations, Himawari's AHI, precipitation estimated from microwaves, and RH estimated from GPM/DPR have a large impact. The combined DFS of each satellite accounts for roughly 30% of the total DFS. Although a variety of observations are assimilated, it is clear that satellite observations contribute to create the initial conditions for the MSM. Figure 12b shows the DFS per observation (DFS/p). It can be seen that in situ observations such as radiosonde and aircraft observations have a large impact per observation. Focusing on remote sensing observations, the DFS/p of satellite observations and those of Doppler velocity observations are relatively small, and that of DPR is large. Since the brightness temperature of satellite and the Doppler velocity have huge number of observations, the impact per observation is not large. On the other hand, the number of observations of DPR is not as large as those observations. In addition, DPR is assimilated as a RH profile (Ikuta et al., 2021), which has 3D information of water vapor in the precipitation system. Especially over the ocean, because such RH profiles are unique in our system, the DPR has a relatively large impact per observation compared to other observational data. For example, in the Météo-France regional DA system, Brousseau et al. (2014) showed that radar DFS is large and radiosonde DFS/p is relatively large, which is similar to our DA system. Fig. 12

4.2 Analysis forecast cycle

a. JNoVA and ASUCA-Var

To compare the performance of JNoVA and ASUCA-Var, with a particular focus on MA, an experiment was conducted using the mesoscale NWP system. The JNoVA experiment uses JNoVA as the data assimilation system. The setup of JNoVA is described in Section 2 of the outline of NWP at JMA (Japan Meteorological Agency, 2019). The ASUCA-Var experiment uses ASUCA-Var as the data assimilation system. The forecast model for both experiments was ASUCA, MSM2003 (Ikuta et al., 2020) version.

The major differences between JNoVA and ASUCA-Var are shown in Table 3. The analysis variables of ASUCA-Var are the analysis variables of JNoVA with the addition of the underground elements T_{g} and W_{g} (see subsection 2.2). $\mathbf{B}_\mathrm{v}$ of JNoVA is independent of location and time, while $\mathbf{B}_\mathrm{v}$ of ASUCA-Var depends on the initial time and surface type (see subsection 2.3). The same $\mathbf{B}_\mathrm{h}$ is used for both, however, JNoVA uses Cholesky decomposition and ASUCA-Var uses the recursive filter (see subsection 2.7a). The model operators used as strong constraints are JMA-NHM in JNoVA and ASUCA in ASUCA-Var. NL is used for the forward calculation method in the inner loop of JNoVA and TL is used in ASUCA-Var. The maximum number of iterations to find the minimum of cost function in JNoVA is 35, and the total number of iterations for ASUCA-Var is 50-time. The breakdown of the number of iterations for ASUCA-Var is as described in subsection 3.1a. For parallel computation, JNoVA divides the domain into one-dimensional strips, while ASUCA-Var divides the domain into two-dimensional blocks (see subsection 2.9). Table 3

b. Comparison of performances

The experimental periods are June 18 to July 23, 2018; and December 23, 2018, to January 27, 2019. The JNoVA and ASUCA-Var experiments assimilate the same kind of observations. However, the treatment of observations such as VarQC and VarBC is different. Figure 13 shows the number of assimilated observation related to VarQC and VarBC at each initial time in JNoVA experiment and ASUCA-Var experiment. Figure 13a shows conventional observations which have VarQC weight larger than 0.25. In Fig. 13a, the reason why there are more observations at 0300 UTC than at other initial times is that there are more radiosonde and aircraft observations, and the reason why there are fewer observations at 1800–2100 UTC is that those initial times are late at night in local time, thus the number of aircraft observations is few. Figure 13b shows the number of observations of T_{B} for satellite observations with VarBC in the ASUCA-Var experiment and without VarBC in the JNoVA experiment. At 0000 UTC and 1200 UTC, the number of observations is larger than other initial times, because the NOAA and DMSP satellites cover the analysis region regularly. For both the conventional observation with VarQC and the satellite observations related VarBC, the number of assimilated observations in the ASUCA-Var is slightly higher than the number of assimilated observations in the JNoVA, but the difference is small compared to the overall number of assimilated observations. Fig. 13

In the JNoVA experiment, satellite brightness temperature uses the variational bias correction coefficient of the global data assimilation system, which provides the initial condition for the global model at JMA. Conversely, in the ASUCA-Var experiment satellite observation bias is corrected by the variational bias correction of MA. Figure 14 shows a boxplot of the observed brightness temperature minus the first guess of brightness temperature. The observations shown in Fig. 14 are GPM/GMI, Metop-B/MHS, Metop-B/AMSU-A, and Himawari-8/AHI. The channels 3, 5, 12 and 13 of GMI without bias correction have large bias, however JNoVA and ASUCA-Var correct the bias successfully. In JNoVA, the channels 6 and 8 of GMI (Fig. 14a), the channels 3–5 of Metop-B/MHS (Fig. 14b), the channels 6–7 of Metop-B/AMSUA (Fig. 14c), and the channels 2–3 of Himawari-8/AHI (Fig. 14d) have larger bias than uncorrected observation. However, all of them are very well corrected in ASUCA-Var. From the above, in the JNoVA experiment, the brightness temperature bias is not fully corrected, and the divergence of the bias correction factor from the global analysis is the cause of bias in some channels. On the other hand, in the ASUCA-Var experiment, bias is corrected as expected by the variational bias correction. Fig. 14

The impact on the forecast is shown next. Figure 15 shows the bias score and equitable threat score (ETS) of the 3-hour accumulated precipitation forecast against R/A. These scores are averaged over the lead time of 3–39 hours. In the summer experiment from 0000 UTC 18 Jun 2018 to 2100 UTC 23 July 2018, the bias scores under the threshold 5 mm in JNoVA experiment indicates overprediction (Fig. 15a), however the ASUCA-Var experiment significantly improves such overprediction (Fig. 15b). In Fig. 15c, the difference of ETS shows significant improvement in ASUCA-Var at all thresholds. In the winter experiment from 0000 UTC 23 December 2017 to 2100 UTC 27 January 2018, the difference of ETS indicates that the precipitation forecast in ASUCA-Var experiment is significantly improved under the threshold of 5 mm (Fig. 15f). Fig. 15

Figure 16 shows the results of the verification of 3-hour accumulated precipitation using Fractions Skill Score (FSS: Roberts and Lean, 2008). FSS is a scale-dependent score, and verification using FSS is expected to reduce misleading influence due to double penalty (Gilleland et al., 2009). The ASUCA-Var experiment in the summer period showed that precipitation forecasts at threshold of 1 mm were significantly worse at spatial scales of about 300 km, however significantly better at spatial scales under about 100 km (Fig. 16a). At the threshold of 5 mm, the precipitation forecast of ASUCA-Var experiment improved significantly at a spatial scale under about 100 km (Fig. 16b). In addition, over the threshold of 10 mm, FSS shows that ASUCA-Var experiment is improved significantly at all spatial scales (Fig. 16c–e). In the winter period, the ASUCA-Var experiment is significantly improved at all scales under the threshold of 30 mm (Fig. 16f–i). Fig. 16

The accuracy of the precipitation forecast was verified by using the improvement ratio of ETS, defined as

$$I_{ETS} = 2 \times \frac{\langle ETS_{\text{ASUCA-Var}} - ETS_{\text{JNoVA}} \rangle}{f_{ci}\left(ETS_{\text{ASUCA-Var}} - ETS_{\text{JNoVA}}\right)}, \tag{124}$$

where $\langle \cdot \rangle$ denotes the mean and $f_{ci}(\cdot)$ denotes the 95% confidence interval. f_{ci} was obtained by the block bootstrap method, and ETS was obtained using R/A as the reference value.

Forecast against radiosonde and SYNOP were verified by the improvement ratio using the root mean square error (RMSE). Note that most of these observations were assimilated in MA. The indices are given by

$$I_{RMSE} = 2 \times \frac{\langle RMSE_{\text{JNoVA}} - RMSE_{\text{ASUCA-Var}} \rangle}{f_{ci} \left(RMSE_{\text{JNoVA}} - RMSE_{\text{ASUCA-Var}} \right)}. \tag{125}$$

In Eqs. (124)-(125), the coefficient 2 is a scaling factor that simply sets the significance value to ± 1. If these indicators are greater (smaller) than or equal to 1, they indicate statistically significant improvement (deterioration). Figures 17a and 17b show the indexes in summer and winter experiments. Verified elements are 3-hour accumulated precipitation; specific humidity, temperature, wind speed and geopotential height of radiosonde; screen-level specific humidity at an altitude 1.5 m, screen-level temperature at an altitude 1.5 m, screen-level wind speed at an altitude 10 m, surface pressure, and solar radiation. Fig. 17

First, in summer period (Fig. 17a), precipitation prediction was improved in the ASUCA-Var experiment. Specific humidity of lower troposphere (925–850 hPa) was degraded in some parts of the initial time, but there was no significant degradation in the almost all lead times of forecast. Temperature, wind speed, and geopotential height were improved at almost all times. Surface pressure, screen-level specific humidity, screen-level temperature, screen-level wind speed, and solar radiation have improved also in almost all lead times. The reason for the difference in the sensitivity of specific humidity between the screen-level and the lower-atmosphere is that the screen level is more affected by the underground control variables which are newly added in ASUCA-Var. Next, in winter period (Fig. 17b), indices of precipitation forecasts are improved mainly under the threshold of 5 mm and after T+24h. The improvement in precipitation forecast is greater in summer than in winter. Specific humidity at upper troposphere (200 hPa) was degraded in some lead times of forecast, however that of lower troposphere was improved. The improvement in forecast accuracy for tropospheric temperature, wind speed, and geopotential height is greater in winter than in summer. Surface pressure, screen-level specific humidity, screen-level temperature, and solar radiation have improved in winter. The screen-level wind speed was improved at the initial time, and was worsened afterwards. Consequently, the absolute value of wind speed RMSE became larger.

The performance of 4D-Var, with the model as a strong constraint, naturally also depends on the characteristics of the model's performance. Thus, the improvement in prediction shown here is due to not only the enhancement of data assimilation methods, such as the newly added control variables, background errors, and variational bias correction, but also in no small part to differences between the inner and outer models.

5. Concluding remarks

In this paper, the data assimilation system for the JMA regional model was reviewed. The JMA has been operating ASUCA-Var which is a variational data assimilation system based on the non-hydrostatic model ASUCA in LA since 0300 UTC 29 January 2015, and in MA since 0000 UTC 25 March 2020. As data assimilation methods, 3D-Var and 4D-Var versions are adopted as initial value generation methods for LFM in LA and MSM in MA, respectively. Applying several refinements such as control variables, background errors, and manually coded TL and AD models, and equipped with advanced techniques including basic field updates, VarQC, and VarBC, ASUCA-Var attained a remarkable improvement in operational regional NWP forecasts.

With respect to the next steps, flow dependency for the background error is limited in the current MA and LA. Thus, we are developing these systems to be extended to a hybrid data assimilation system using ensemble forecasts. The numerical prediction centers that currently use variational methods are also using hybrid assimilation with ensemble forecasts in their current operations or plan to do so in the near future (Gustafsson et al., 2018).

To forecast precipitation systems accurately, it is also important to make hydrometeors control variables. Because the background error of hydrometeors is strongly dependent on the meteorological situation, a flow-dependent background error is required. Ikuta (2017b) has been developing a direct assimilation of radar reflectivity using a hybrid data assimilation method with hydrometeors as control variables. Currently, ASUCA-Var adopts a strongly constrained 4D-Var, which assumes that there is no error in the model. However, NWP model is not perfect in practice, thus the bias of individual observations corrected by VarBC also includes model bias. Although weakly constrained 4D-Var (e.g., Trémolet, 2006) may be adopted in the future to account for model errors into J^{b} and other term (e.g., systematic error term) as well as J^{df}, current model errors are clear and large compared to observation errors, and the best way to resolve such clear errors is to improve the model by identifying the sources of errors.

Finally, we remark on the advantages of ASUCA-Var in terms of sustainable development practices. ASUCA-Var is coded with a strong awareness of the fate of 4D-Var, where the TL has to follow the model updates. This development manner, which prevents the model from leaving behind the data assimilation system, contributes to maintaining the consistency of the model used in the analysis forecast cycle. Furthermore, the packaging of the observation operators will also lead to more efficient development through unit testing. These innovations will promote sustainable development. In terms of forecast accuracy, ASUCA-Var, which has a high affinity between assimilation and models, can quickly introduce the benefits of model sophistication in the assimilation system, and assimilation can produce effects that are consistent with the model, resulting in improved forecast accuracy. The improvement in forecasting accuracy reported by Ikuta et al. (2020) is a result of such enhancements in the development of ASUCA-Var. In the future, data assimilation of operational regional models is likely to move to higher resolution and target phenomena with stronger nonlinearity. ASUCA-Var will be a platform for the development of fundamental technologies to handle these complex relationships in an integrated manner and improve prediction accuracy.

Acknowledgements

We gratefully acknowledge colleagues at the Japan Meteorological Agency for the discussions and material provided for this article. Additionally, we are grateful to Dr. Takuya Kawabata, Dr. Ken Sawada, Dr. Daisuke Hotta, Dr. Kozo Okamoto, Dr. Hiromu Seko of Meteorological Research Institute, and Dr. Kazuo Saito of Atmosphere and Ocean Research Institute for the scientific discussions. Many constructive comments from two anonymous reviewers are also greatly appreciated to improve the paper.

References

Adams, L. M., and J. M. Ortega, 1982: A multi-color SOR method for parallel computation. *Icpp*, Citeseer, 53–56.

Anderson, E., and H. Järvinen, 1999: Variational quality control. *Quart. J. Roy. Meteor. Soc.*, **125**, 697–722, doi:10.1002/qj.49712555416.

Aranami, K., and Coauthors, 2015: A new operational regional model for convection-permitting numerical weather prediction at JMA. *CAS/JSC WGNE Res. Activ. Atmos. Oceanic Modell.*, **45**, 05.05–05.06. Available at http://bluebook.meteoinfo.ru/uploads/2015/individual-articles/05_Aranami_Kohei_asuca.pdf.

Bannister, R. N., 2008: A review of forecast error covariance statistics in atmospheric variational data assimilation. I: Characteristics and measurements of forecast error covariances. *Quart. J. Roy. Meteor. Soc.*, **134**, 1951–1970, doi:10.1002/qj.339.

Beljaars, A. C. M., and A. A. M. Holtslag, 1991: Flux parameterization over land surfaces for atmospheric models. *J. Appl. Met. Clim.*, **30**, 327–341, doi:10.1175/1520-0450(1991)030⟨0327:FPOLSF⟩2.0.CO;2.

Benáček, P., and M. Mile, 2019: Satellite bias correction in the regional model ALADIN/CZ: Comparison of different varBC approaches. *Mon. Wea. Rev.*, **147**, 3223–3239, doi:10.1175/MWR-D-18-0359.1.

Box, G. E. P., and D. R. Cox, 1964: An analysis of transformations. *J. Roy. Stat. Soc.*, **26**, 211–252.

Brousseau, P., G. Desroziers, F. Bouttier, and B. Chapnik, 2014: A posteriori diagnostics of the impact of observations on the AROME-france convective-scale data assimilation system. *Quart. J. Roy. Meteor. Soc.*, **140**, 982–994, doi:10.1002/qj.2179.

Cameron, J., and W. Bell, 2018: *The testing and implementation of variational bias correction (VarBC) in the Met Office global NWP system.* Weather Science Technical Report No: 631, Met Office, available at https://www.metoffice.gov.uk/research/library-and-archive/publications/science/weather-science-technical-reports.

Cardinali, C., S. Pezzulli, and E. Andersson, 2004: Influence-matrix diagnostic of a data assimilation system. *Quart. J. Roy. Meteor. Soc.*, **130**, 2767–2786, doi:10.1256/qj.03.205.

Chapnik, B., G. Desroziers, F. Rabier, and O. Talagrand, 2006: Diagnosis and tuning of observational error in a quasi-operational data assimilation setting. *Quart. J. Roy. Meteor. Soc.*, **132**, 543–565, doi: 10.1256/qj.04.102.

Courtier, P., J.-N. Thépaut, and A. Hollingsworth, 1994: A strategy for operational implementation of 4D-var, using an incremental approach. *Quart. J. Roy. Meteor. Soc.*, **120**, 1367–1387, doi:10.1002/qj.49712051912.

Dee, D. P., 2004: Variational bias correction of radiance data in the ECMWF system. *ECMWF Workshop on Assimilation of high spectral resolution sounders in NWP, 28 June - 1 July 2004*, Shinfield Park, Reading, ECMWF, URL https://www.ecmwf.int/node/8930.

Dee, D. P., and A. M. da Silva, 2003: The choice of variable for atmospheric moisture analysis. *Mon. Wea. Rev.*, **131**, 155–171, doi: 10.1175/1520-0493(2003)131⟨0155:TCOVFA⟩2.0.CO;2.

Fujita, T., 2010: Flow-dependent background error. *Separate vol. ann. rep. NPD*, **56**, 78–83 (in Japanese).

Fukuda, J., T. Fujita, Y. Ikuta, Y. Ishikawa, and K. Yoshimoto, 2011: Development of JMA local analysis. *CAS/JSC WGNE Res. Activ. Atmos. Oceanic Modell.*, **41**, 01.07–01.08. Available at http://bluebook.meteoinfo.ru/uploads/2011/individual-articles/01_Fukuda_Junya_Development_of_JMA_Local_Analysis.pdf.

Gauthier, P., and J.-N. Thépaut, 2001: Impact of the digital filter as a weak constraint in the preoperational 4DVAR assimilation system of Météo-france. *Mon. Wea. Rev.*, **129**, 2089–2102, doi:10.1175/1520-0493(2001)129⟨2089:IOTDFA⟩2.0.CO;2.

Gilleland, E., D. Ahijevych, B. G. Brown, B. Casati, and E. E. Ebert, 2009: Intercomparison of spatial forecast verification methods. *Wea. Forecasting*, **24**, 1416–1430, doi:10.1175/2009WAF2222269.1.

Gustafsson, N., 1992: Use of a digital filter as weak constraint in variational data assimilation. URL https://www.ecmwf.int/node/9692.

Gustafsson, N., and Coauthors, 2018: Survey of data assimilation methods for convective-scale numerical weather prediction at operational centres. *Quart. J. Roy. Meteor. Soc.*, **144**, 1218–1256, doi:10.1002/qj.3179.

Hara, T., K. Kawano, K. Aranami, Y. Kitamura, M. Sakamoto, H. Kusabiraki, C. Muroi, and J. Ishida, 2012: Development of Physics Library and its application to ASUCA. *CAS/JSC WGNE Res. Activ. Atmos. Oceanic Modell.*, **42**, 05.05–05.06. Available at http://bluebook.meteoinfo.ru/uploads/2012/individual-articles/05_Hara_Tabito_physlib_asuca.pdf.

Hirahara, Y., O. H., and M. M., 2017: Assimilation of GNSS RO data into JMA's mesoscale NWP system. *CAS/JSC WGNE Res. Activ. Atmos. Oceanic Modell.*, **47**, 01.15–01.16. Available at http://bluebook.meteoinfo.ru/uploads/2017/docs/01_Hirahara_Yoichi_GNSS_RO_Assimilation.pdf.

Honda, Y., M. Nishijima, K. Koizumi, Y. Ohta, K. Tamiya, T. Kawabata, and T. Tsuyuki, 2005: A pre-operational variational data assimilation system for a non-hydrostatic model at the Japan Meteorological Agency: formulation and preliminary results. *Quart. J. Roy. Meteor. Soc.*, **131**, 3465–3475, doi:10.1256/qj.05.132.

Honda, Y., and K. Sawada, 2009: Upgrade of the operational mesoscale 4D-Var at the Japan Meteorological Agency. *CAS/JSC WGNE Res. Activ. Atmos. Oceanic Modell.*, **39**, 01.11–01.12. Available at http://bluebook.meteoinfo.ru/uploads/2009/individual-articles/01_Honda_Yuki_jnova.pdf.

Honda, Y., and K. Sawada, 2010: Operational msoscale analysis system. *Separate vol. ann. rep. NPD*, **56**, 25–30 (in Japanese).

Ide, K., P. Courtier, M. Ghil, and A. C. Lorenc, 1997: Unified notation for data assimilation : Operational, sequential and variational. *J. Meteor. Soc. Japan*, **75**, 181–189, doi:10.2151/jmsj1965.75.1B_181.

Ikuta, Y., 2017a: Assimilation of satellite soil moisture contents and clear-sky radiance in operational local NWP system at JMA. JpGU-AGU Joint Meeting 2017, 20–24 May, 2017, Makuhari, Japan.

Ikuta, Y., 2017b: Meso-scale hybrid data assimilation using adjoint-model including 3-ice cloud microphysic. RIKEN International Symposium on Data Assimilation 2017, 27 February–2 March, 2017, Kobe, Japan. Available at http://www.data-assimilation.riken.jp/risda2017/program/abstracts/pdf/05_1_Y.Ikuta.pdf (accessed on 18 August 2021).

Ikuta, Y., and Y. Honda, 2011: Development of 1D+4DVAR data assimilation of radar reflectivity in JNoVA. *CAS/JSC WGNE Res. Activ. Atmos. Oceanic Modell.*, **41**, 05.09–05.10. Available at http://bluebook.meteoinfo.ru/uploads/2011/individual-articles/01_Ikuta_Yasutaka_WGNE2011_1D4DVAR.pdf.

Ikuta, Y., K. Okamoto, and T. Kubota, 2021: One-dimensional maximum-likelihood estimation for spaceborne precipitation radar data assimilation. *Quart. J. Roy. Meteor. Soc.*, **147**, 858–875, doi:10.1002/qj.3950.

Ikuta, Y., and Coauthors, 2020: A new data assimilation system and upgrading of physical processes in JMA's meso-scale NWP system. *CAS/JSC WGNE Res. Activ. Earth system Modell.*, **50**, 01.07–01.08. Available at http://bluebook.meteoinfo.ru/uploads/2020/docs/01_Ikuta_Yasutaka_MAMSM2003.pdf.

Ishida, J., C. Muroi, K. Kawano, and K. Y., 2010: Development of a new nonhydrostatic model "ASUCA" at JMA. *CAS/JSC WGNE Res. Activ. Atmos. Oceanic Modell.*, **40**, 05.11–05.12. Available at http://bluebook.meteoinfo.ru/uploads/2010/individual-articles/05_Ishida_Junichi_wgne_ishida_muroi_kawano_kitamura_asuca.pdf.

Ishida, J., C. Muroi, and A. Y., 2009: Development of a new dynamical core for the nonhydrostatic model. *CAS/JSC WGNE Res. Activ. Atmos. Oceanic Modell.*, **39**, 05.09–05.10. Available at http://bluebook.meteoinfo.ru/uploads/2009/individual-articles/05_Ishida_Junichi_WGNE_ishida_muroi_aikawa_asuca.pdf.

Ishikawa, Y., 2010: Data assimilation of GPS precipitable water vapor into the JMA mesoscale numerical weather prediction model. *CAS/JSC WGNE Res. Activ. Atmos. Oceanic Modell.*, **34**, 01.13–01.14. Available at http://bluebook.meteoinfo.ru/uploads/2010/individual-articles/01_Ishikawa_Yoshihiro___12487.pdf.

Ishikawa, Y., and K. Koizumi, 2002: One month cycle experimentsof the JMA mesoscale 4-dimensional variational data assimi-lation (4D-Var) system. *CAS/JSC WGNE Res. Activ. Atmos. Oceanic Modell.*, **32**, 01.26–01.27. Available at http://bluebook.meteoinfo.ru/uploads/2002/individual-articles/01_ishikawa_yoshihiro.pdf.

Ishikawa, Y., and K. Koizumi, 2006: Doppler radar wind data assimilation with JMA Meso 4D-VAR. *CAS/JSC WGNE Res. Activ. Atmos. Oceanic Modell.*, **36**, 01.11–01.12. Available at http://bluebook.meteoinfo.ru/uploads/2006/individual-articles/01_Ishikawa_Yoshihiro_Doppler_Meso_4D-Var.pdf.

Ito, K., M. Kunii, T. Kawabata, K. Saito, K. Aonashi, and L. Duc, 2016: Mesoscale hybrid data assimilation system based on JMA nonhydrostatic model. *Mon. Wea. Rev.*, **144**, 3417–3439, doi: 10.1175/MWR-D-16-0014.1.

Japan Meteorological Agency, 2019: *Outline of the operational numerical weather prediction at the Japan Meteorological Agency. Appendix to WMO Technical Progress Report on the Global Data-processing and Forecasting System and Numerical Weather Prediction Research.* Japan Meteorological Agency, 229 pp., available at https://www.jma.go.jp/jma/jma-eng/jma-center/nwp/outline2019-nwp/index.htm.

Kain, J. S., and J. M. Fritsch, 1990: A one-dimensional entraining/detraining plume model and its application in convective parameterization. *J. Atmos. Sci.*, **47**, 2784–2802, doi:10.1175/1520-0469(1990)047⟨2784:AODEPM⟩2.0.CO;2.

Kawabata, T., K. Ito, and K. Saito, 2014: Recent progress of the NHM-4DVAR towards a super-high resolution data assimilation. *SOLA*, **10**, 145–149, doi:10.2151/sola.2014-030.

Kawabata, T., M. Kunii, K. Bessho, T. Nakazawa, N. Kohno, Y. Honda, and K. Sawada, 2012: Reanalysis and reforecast of typhoon Vera (1959) using a mesoscale four-dimensional variational assimilation system. *J. Meteor. Soc. Japan*, **90**, 467–491, doi:10.2151/jmsj.2012-403.

Kawabata, T., T. Kuroda, H. Seko, and K. Saito, 2011: A cloud-resolving 4DVAR assimilation experiment for a local heavy rainfall event in the tokyo metropolitan area. *Mon. Wea. Rev.*, **139**, 1911–1931, doi:10.1175/2011MWR3428.1.

Kawabata, T., H. Seko, K. Saito, T. Kuroda, K. Tamiya, T. Tsuyuki, Y. Honda, and Y. Wakazuki, 2007: An assimilation and forecasting experiment of the nerima heavy rainfa11 with a cloud-resolving nonhydrostatic 4-dimensional variational data assimilation system. *J. Meteor. Soc. Japan*, **85**, 255–276, doi:10.2151/jmsj.85.255.

Kazumori, M., 2014: Satellite radiance assimilation in the JMA operational mesoscale 4DVAR system. *Mon. Wea. Rev.*, **142**, 1361–1381, doi: 10.1175/MWR-D-13-00135.1.

Klinker, E., F. Rabier, G. Kelly, and J.-F. Mahfouf, 2000: The ecmwf operational implementation of four-dimensional variational assimilation. III: Experimental results and diagnostics with operational configuration. *Quart. J. Roy. Meteor. Soc.*, **126**, 1191–1215, doi: 10.1002/qj.49712656417.

Koizumi, K., Y. Ishikawa, and T. Tsuyuki, 2005: Assimilation of precipitation data to the JMA mesoscale model with a four-dimensional variational method and its impact on precipitation forecasts. *SOLA*, **1**, 45–48, doi:10.2151/sola.2005-013.

Kunii, M., H. Seko, M. Ueno, Y. Shoji, and T. Tsuda, 2012: Impact of assimilation of GPS radio occultation refractivity on the forecast of typhoon Usagi in 2007. *J. Meteor. Soc. Japan*, **90**, 255–273, doi: 10.2151/jmsj.2012-207.

Liu, D. C., and J. Nocedal, 1989: On the limited memory BFGS method for large scale optimization. *Mathematical Programming*, **45**, 503–528, doi:10.1007/BF01589116.

Lynch, P., 1997: The dolph–chebyshev window: A simple optimal filter. *Mon. Wea. Rev.*, **125**, 655–660, doi:10.1175/1520-0493(1997)125⟨0655:TDCWAS⟩2.0.CO;2.

Mahfouf, J.-F., 1999: Influence of physical processes on the tangent-linear approximation. *Tellus A: Dynamic Meteorology and Oceanography*, **51**, 147–166, doi:10.3402/tellusa.v51i2.12312.

Mahfouf, J.-F., and F. Rabier, 2000: The ECMWF operational implementation of four-dimensional variational assimilation. II: Experimental results with improved physics. *Quart. J. Roy. Meteor. Soc.*, **126**, 1171–1190, doi:10.1002/qj.49712656416.

Nagata, K., 2011: Quantitative precipitation estimation and quantitative precipitation forecasting by the Japan Meteorological Agency. *Technical Review of RSMC Tokyo*, **13**, 37–50.

Nakanishi, M., and H. Niino, 2004: An improved mellor–yamada level-3 model with condensation physics: Its design and verification. *Bound.-Layer Meteor.*, **112**, 1–31, doi:10.1023/B:BOUN.0000020164.04146.98.

Nocedal, J., 1980: Updating quasi-newton matrices with limited storage. *Math. Comput.*, **35**, 773–782.

Parrish, D. F., and J. C. Derber, 1992: The national meteorological center's spectral statistical-interpolation analysis system. *Mon. Wea. Rev.*, **120**, 1747–1763, doi:10.1175/1520-0493(1992)120⟨1747:TNMCSS⟩2.0.CO;2.

Polavarapu, S., M. Tanguay, and L. Fillion, 2000: Four-dimensional variational data assimilation with digital filter initialization. *Mon. Wea. Rev.*, **128**, 2491–2510, doi:10.1175/1520-0493(2000)128⟨2491:FDVDAW⟩2.0.CO;2.

Purser, R. J., W.-S. Wu, D. F. Parrish, and N. M. Roberts, 2003: Numerical aspects of the application of recursive filters to variational statistical analysis. part I: Spatially homogeneous and isotropic gaussian covariances. *Mon. Wea. Rev.*, **131**, 1524–1535, doi:10.1175//1520-0493(2003)131⟨1524:NAOTAO⟩2.0.CO;2.

Rabier, F., H. Järvinen, E. Klinker, J.-F. Mahfouf, and A. Simmons, 2000: The ECMWF operational implementation of four-dimensional variational assimilation. I: Experimental results with simplified physics. *Quart. J. Roy. Meteor. Soc.*, **126**, 1143–1170, doi:10.1002/qj.49712656415.

Roberts, N. M., and H. W. Lean, 2008: Scale-selective verification of rainfall accumulations from high-resolution forecasts of convective events. *Mon. Wea. Rev.*, **136**, 78–97, doi:10.1175/2007MWR2123.1.

ROM SAF, 2019: The radio occultation meteorology satellite application facility. URL http://www.romsaf.org.

Saito, K., J. Ishida, K. Aranami, T. Hara, T. Segawa, M. Narita, and Y. Honda, 2007: Nonhydrostatic atmospheric models and operational development at JMA. *J. Meteor. Soc. Japan*, **85B**, 271–304, doi:10.2151/jmsj.85B.271.

Saito, K., and Coauthors, 2006: The operational JMA nonhydrostatic mesoscale model. *Mon. Wea. Rev.*, **134**, 1266–1298, doi:10.1175/MWR3120.1.

Sasaki, Y., 1958: An objective analysis based on the variational method. *J. Meteor. Soc. Japan*, **36**, 77–88, doi:10.2151/jmsj1923.36.3_77.

Sato, Y., 2007: Introduction of variational bias correction technique into the JMA global data assimilation system. *CAS/JSC WGNE Res. Activ. Atmos. Oceanic Modell.*, **37**, 01.19–01.20. Available at http://bluebook.meteoinfo.ru/uploads/2007/individual-articles/01_Sato_Yoshiaki_sato-varbc.pdf.

Saunders, R., and Coauthors, 2018: An update on the RTTOV fast radiative transfer model (currently at version 12). *Geoscientific Model Development*, **11**, 2717–2737, doi:10.5194/gmd-11-2717-2018.

Sawada, K., and Y. Honda, 2008: Initialization. *Separate vol. ann. rep. NPD*, **54**, 68–74 (in Japanese).

Seko, H., T. Kawabata, T. Tsuyuki, H. Nakamura, K. Koizumi, and T. Iwabuchi, 2004: Impacts of GPS-derived water vapor and radial wind measured by Doppler radar on numerical prediction of precipitation. *J. Meteor. Soc. Japan*, **82**, 473–489, doi:10.2151/jmsj.2004.473.

Shoji, Y., M. Kunii, and K. Saito, 2011: Mesoscale data assimilation of myanmar cyclone nargis part II: Assimilation of GPS-derived precipitable water vapor. *J. Meteor. Soc. Japan*, **89**, 67–88, doi:10.2151/jmsj.2011-105.

Talagrand, O., and P. Courtier, 1987: Variational assimilation of meteorological observations with the adjoint vorticity equation. I: Theory. *Quart. J. Roy. Meteor. Soc.*, **113**, 1311–1328, doi:10.1002/qj.49711347812.

Tetens, O., 1930: Über einige meteorologische Begriffe. *Z. Geophys.*, **6**, 297–309.

Trémolet, Y., 2006: Accounting for an imperfect model in 4D-Var. *Quart. J. Roy. Meteor. Soc.*, **132**, 2483–2504, doi:10.1256/qj.05.224.

Trémolet, Y., 2008: Computation of observation sensitivity and observation impact in incremental variational data assimilation. *Tellus A*, **60**, 964–978, doi:10.1111/j.1600-0870.2008.00349.x.

Široká, M., C. Fischer, V. Cassé, R. Brožková, and J.-F. Geleyn, 2003: The definition of mesoscale selective forecast error covariances for a limited area variational analysis. *Meteor. Atmos. Phys.*, **82**, 227–244, doi:10.1007/s00703-001-0588-5.

Wee, T.-K., and Y.-H. Kuo, 2004: Impact of a digital filter as a weak constraint in MM5 4DVAR: An observing system simulation experiment. *Mon. Wea. Rev.*, **132**, 543–559, doi:10.1175/1520-0493(2004)132⟨0543:IOADFA⟩2.0.CO;2.

World Meteorological Organization, 2017: Guide to meteorological instruments and methods of observation, WMO-No 8 (2014 edition, updated 2017). URL http://www.wmo.int/pages/prog/www/IMOP/CIMO-Guide.html.

Yoshimoto, K., 2010: Improvement of conventional observation data usage in the JMA mesoscale 4D-VAR data assimilation system. *CAS/JSC*

WGNE Res. Activ. Atmos. Oceanic Modell., **40**, 01.45–01.46. Available at http://bluebook.meteoinfo.ru/uploads/2010/individual-articles/01_Yoshimoto_Koichi_01_Yoshimoto_Koichi_ConventionalData.pdf.

List of Figures

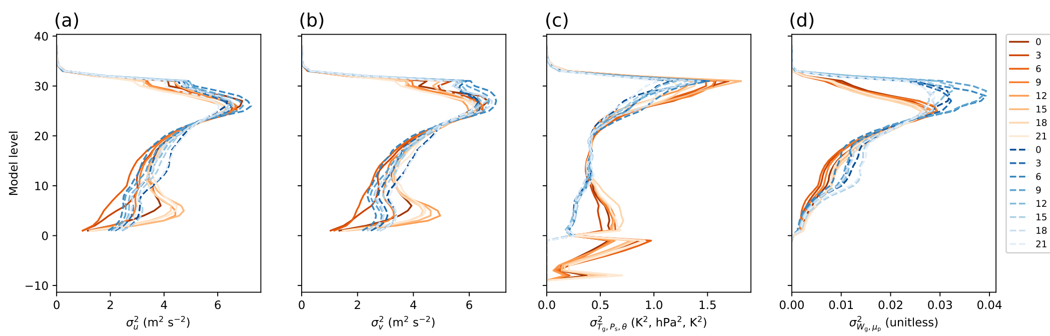

Fig. 1. Background error variance of initial time (UTC) at 3 h intervals. Blue (orange) line shows the background error on sea (land) grid points. The elements are (a) u, (b) v, (c) $(T_{\mathrm{g}}, P_{\mathrm{s}}, \theta)$, and (d) $(W_{\mathrm{g}}, \mu_{\mathrm{p}})$. For convenience, in this figure, T_{g} is placed at -1 level or under, P_{s} is placed at 0 level, and W_{g} is placed at 0 level or under.

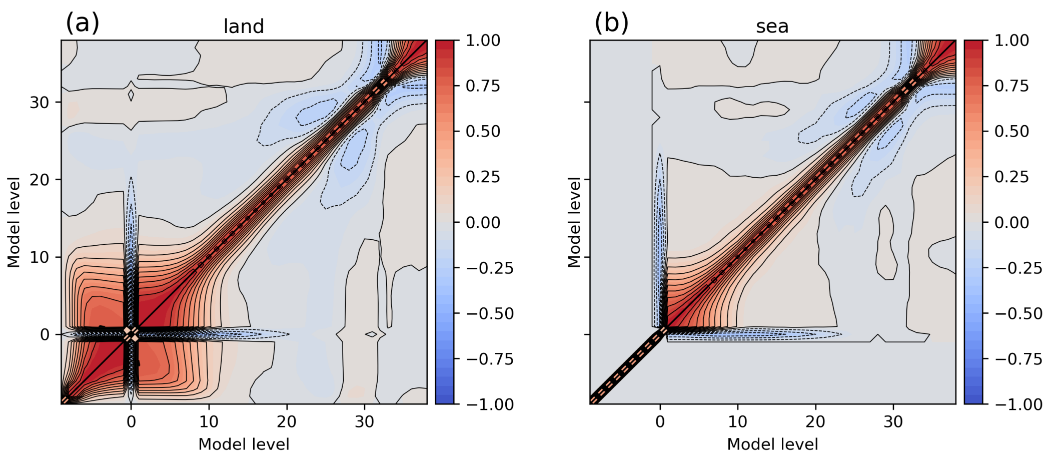

Fig. 2. Background error correlation of $(T_{\mathrm{g}}, P_{\mathrm{s}}, \theta)$ in vertical direction on (a) land grid point and (b) sea grid point at 0600 UTC. T_{g} is placed at -1 level or under, P_{s} is placed at 0 level, and θ is placed at 1 level or above.

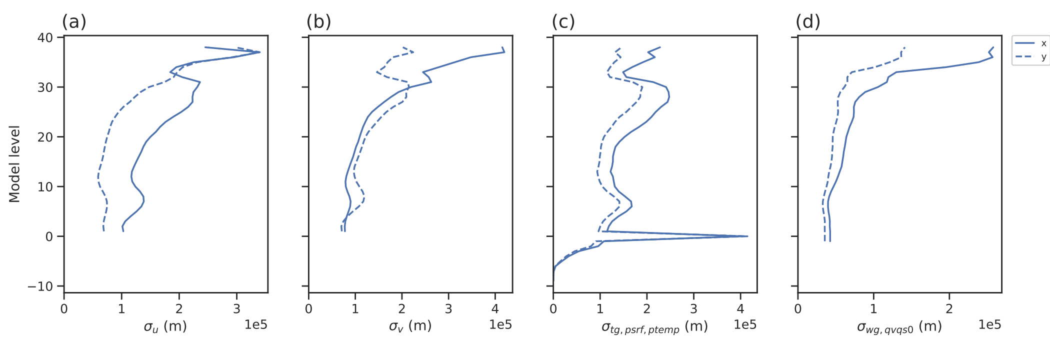

Fig. 3. Horizontal autocorrelation length of background error for (a) u, (b) v, (c) $(T_{\mathrm{g}}, P_{\mathrm{s}}, \theta)$, and (d) $(W_{\mathrm{g}}, \mu_{\mathrm{p}})$ in the x direction (solid line), and in the y direction (dashed line).

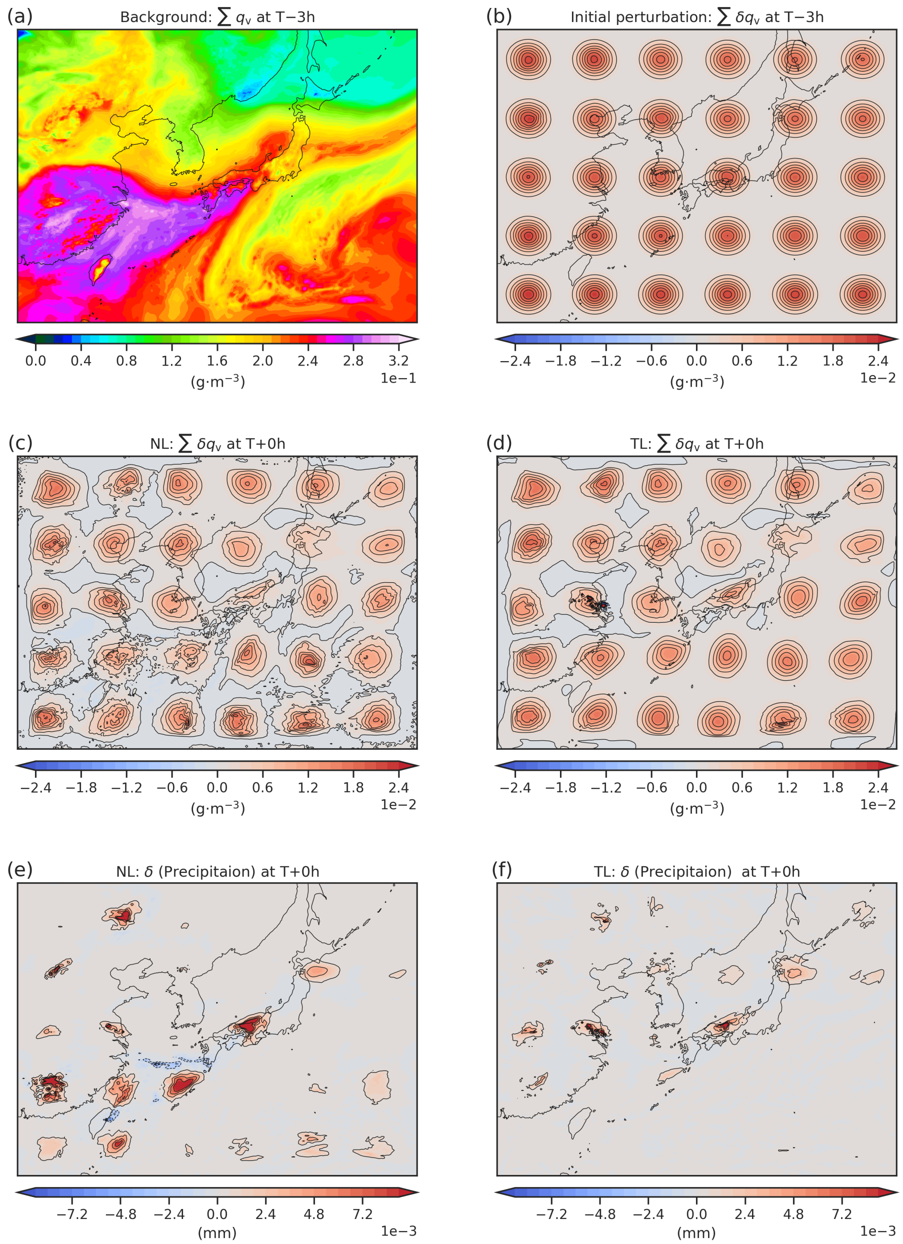

Fig. 4. Comparison between NL perturbation and TL perturbation. (a–d) Integrated q_v in vertical direction and (e–f) precipitation. (a) Background and (b) perturbation at T−3h. (c,e) NL perturbation and (d,f) TL perturbation at T+0h.

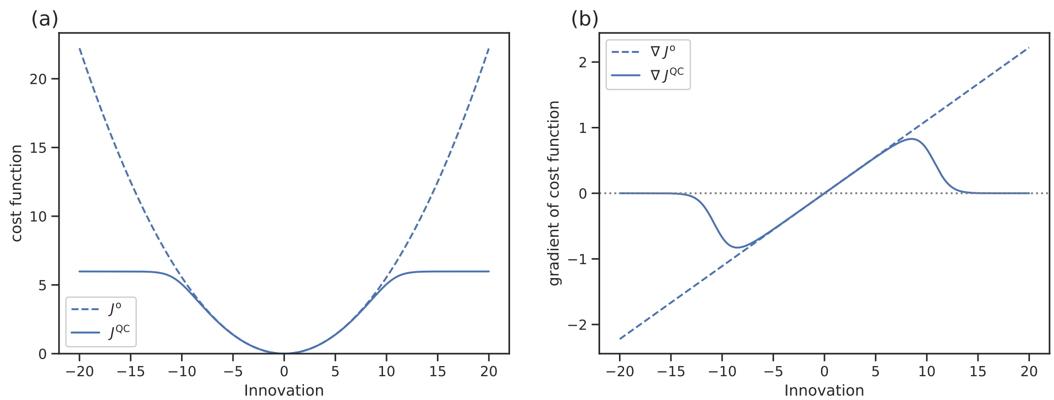

Fig. 5. Single observation case, showing (a) the observation term and (b) gradient of the observation term when $p_{\mathrm{g}} = 0.01$, $d = 5$, and $\sigma_{\mathrm{o}} = 3$. The solid line shows the PDF following the normal distribution, and the dashed line shows the PDF using VarQC.

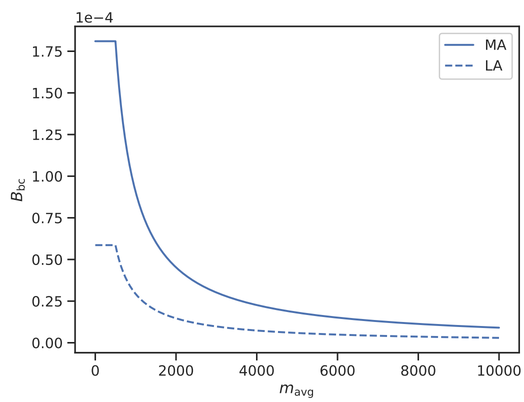

Fig. 6. Background errors in the VarBC term corresponding to the average number of observations when $\sigma_o = 1$. The solid line shows $\mathbf{B}_{bc}$ in MA, and the dashed line shows $\mathbf{B}_{bc}$ in LA.

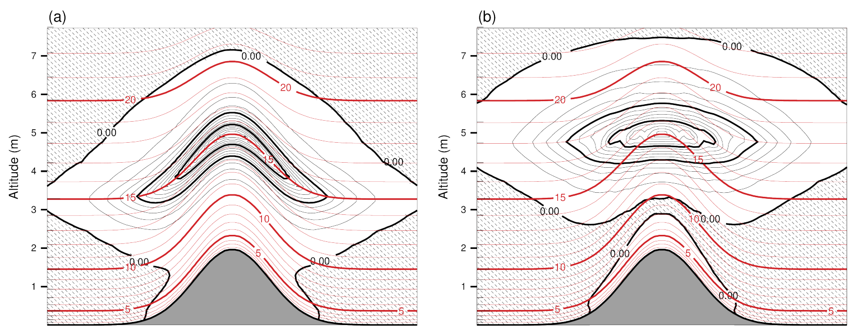

Fig. 7. Analysis increment by temperature observation at an altitude of 5000 m in the center of domain (a) without transformation of the vertical coordinate and (b) with the transformation of the vertical coordinate. The shading shows the terrain, black lines show the analysis increments, and red lines show the model's vertical layers.

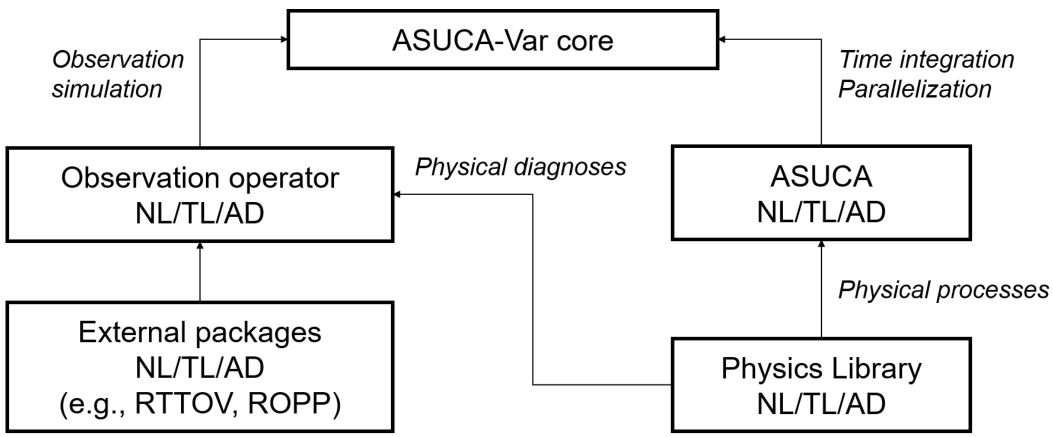

Fig. 8. Structure of ASUCA-Var. The ASUCA-Var core involves preconditioning and optimization.

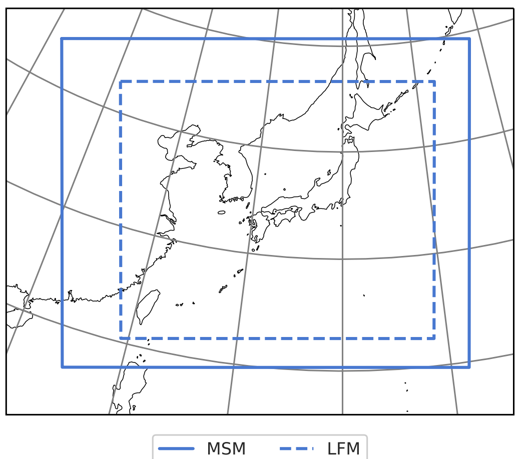

Fig. 9. LFM and MSM domains.

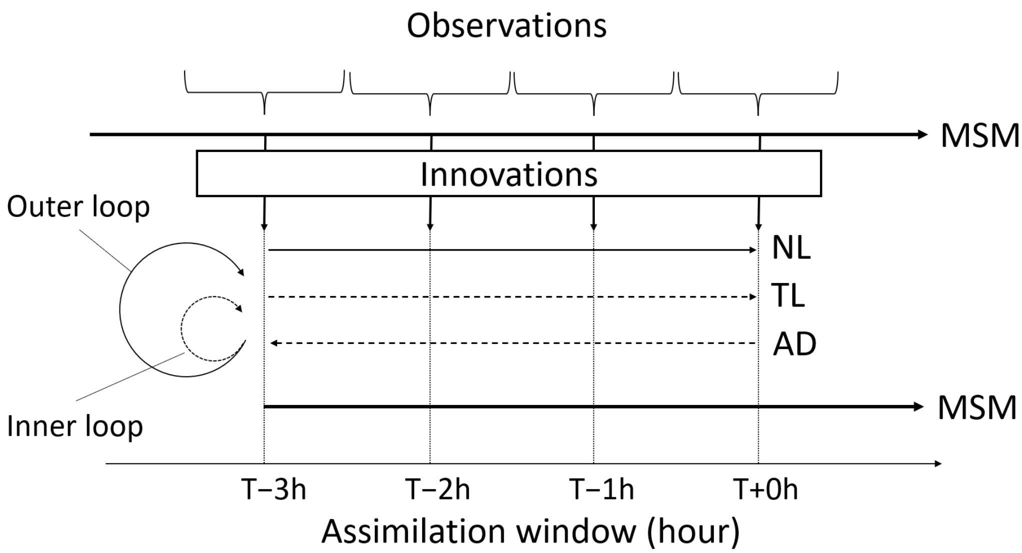

Fig. 10. Flow diagram of MA. NL is the nonlinear model, TL is the tangent-linear model, and AD is the adjoint model. The initial time of MSM is T+0h. The assimilation window is from T−3h to T+0h.

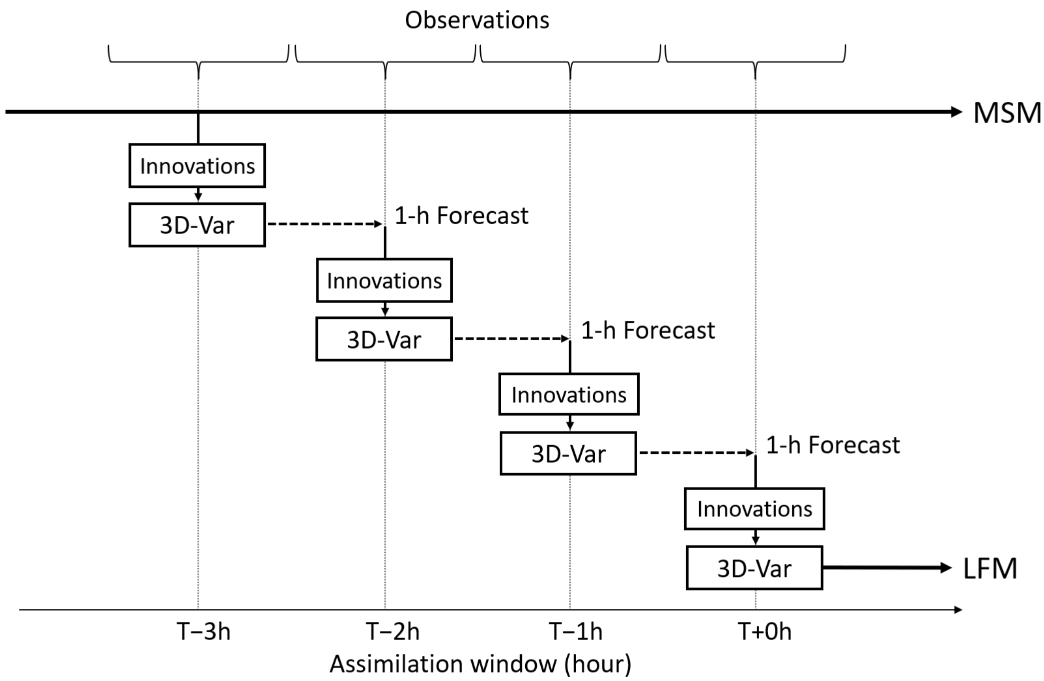

Fig. 11. Flow diagram of LA. The initial time of LFM is T+0h. The assimilation window is from T−3h to T+0h.

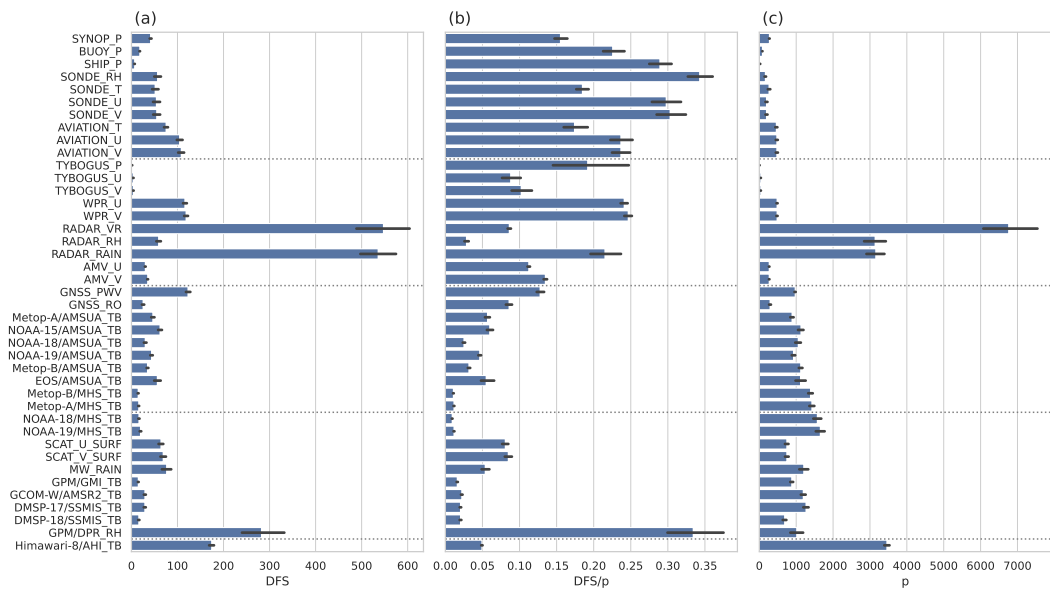

Fig. 12. (a) DFS, (b) DFS per observation, and (c) the average number of observations in MA for each kind of observation: Relative humidity (RH), Temperature (T), x direction wind speed (U), y direction wind speed (V), 1 h accumulated precipitation (RAIN), Doppler velocity (VR), brightness temperature (TB), and pressure at the surface (P).

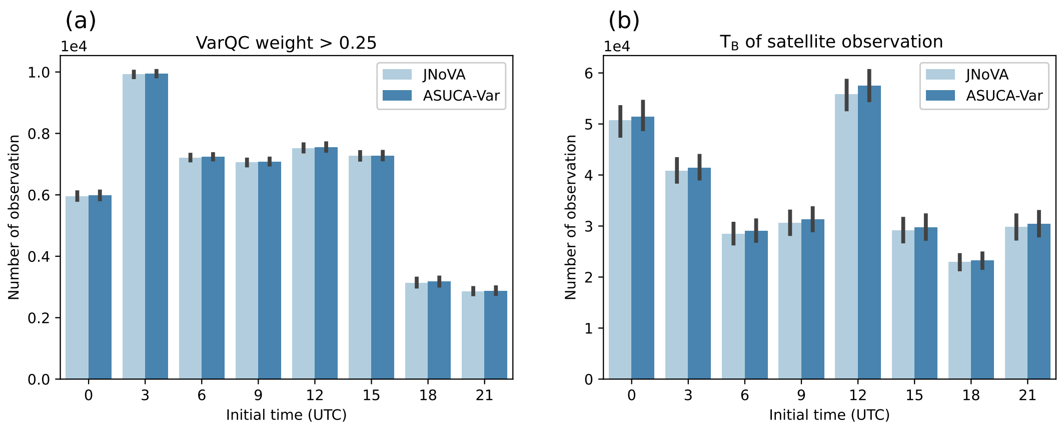

Fig. 13. Number of assimilated observations at each initial time in JNoVA experiment and ASUCA-Var experiment in summer. (a) Conventional observation with VarQC, and (b) T_{B} of satellite observation. Error bars are 95% confidence intervals.

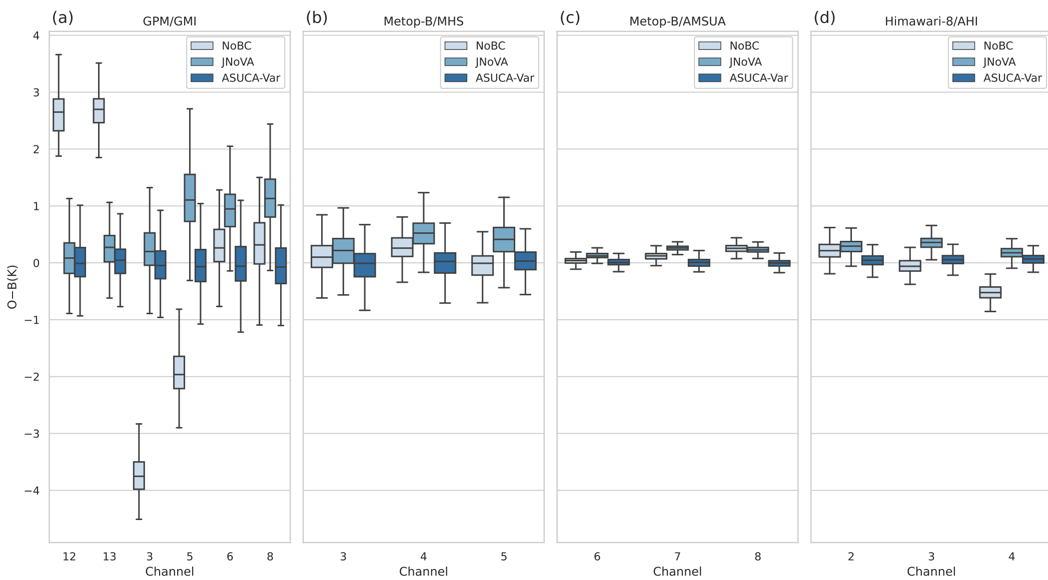

Fig. 14. Boxplots of observation minus background (O−B) for (a) GPM/GMI, (b) Metop-B/MHS, (c) Metop-B/AMSU-A and (d) Himawari/AHI. NoBC indicates O−B with uncorrected observation in ASUCA-Var, JNoVA indicates O−B with VarBC of Global Analysis, and ASUCA-Var indicates O−B with VarBC of MA.

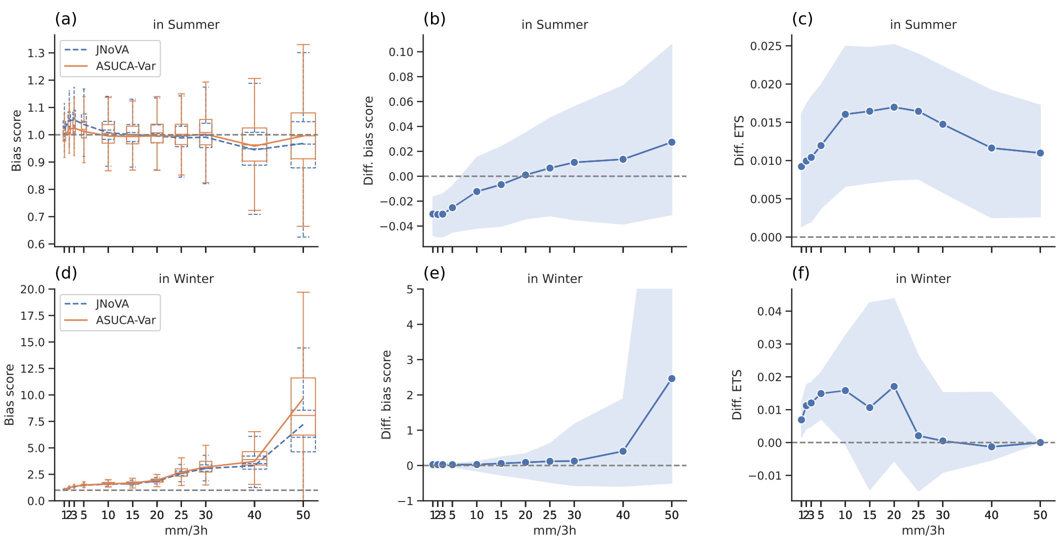

Fig. 15. Precipitation verification in (a–c) summer experiment and (d–f) winter experiment. (a,d) Bias score of ASUCA-Var experiment and JNoVA experiment. (b,e) Difference of bias score and (c,f) difference of ETS; these difference scores indicate score of ASUCA-Var experiment minus that of JNoVA experiment. Shading represents the 95% confidence interval.

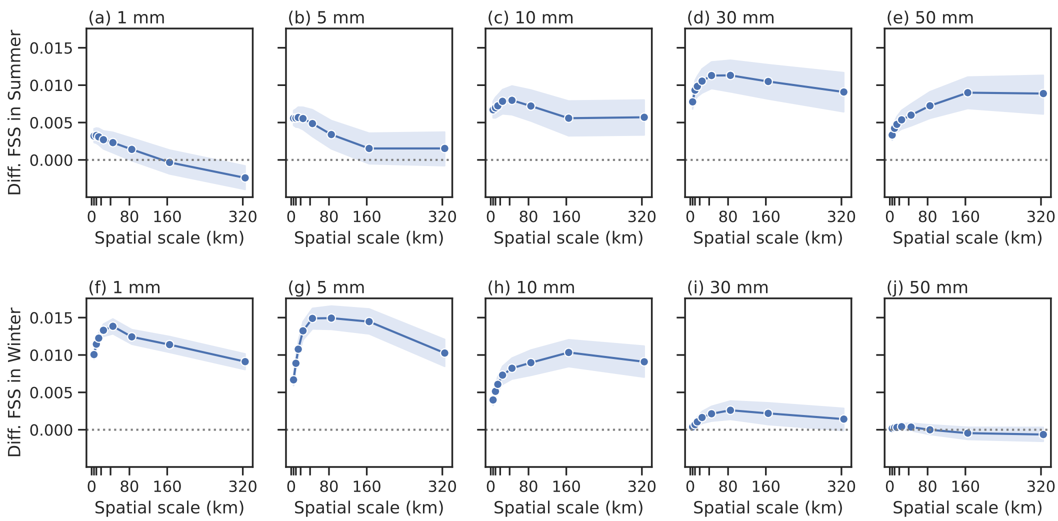

Fig. 16. Verification of 3-hour accumulated precipitation using FSS in (a–e) summer experiment and (f–j) winter experiment. Difference of FSS indicate the FSS of ASUCA-Var experiment minus that of JNoVA experiment. Theresholds are (a,f) 1 mm, (b,g) 5 mm, (c,h) 10 mm, (d,i) 30 mm and (e,j) 50 mm. Spatial scales are 0, 5, 10, 20, 40, 80, 160, and 320 km. Shading represents the 95% confidence interval.

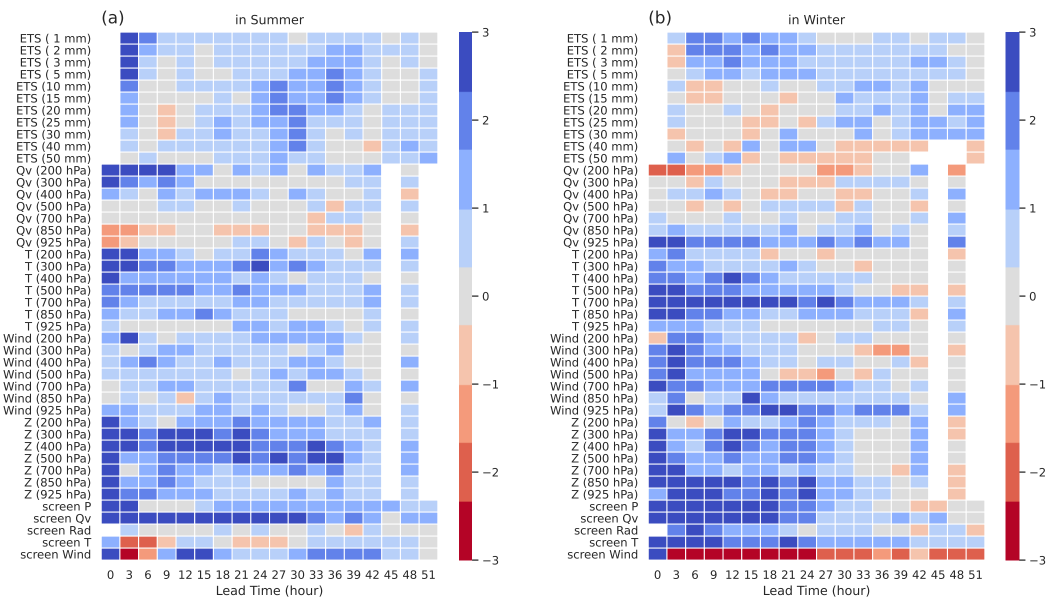

Fig. 17. Indexes of improvement ratio in (a) summer experiment and (b) winter experiment. Shown elements are ETS, specific humidity (Qv), temperature (T), wind speed (Wind), geopotential height (Z), solar radiation (Rad) and pressure (P) at thresholds, pressure-levels or screen-level. |Index| > 1 indicates significance at the 95% level.

List of Tables

Table 1. Configuration of outer/inner models in the meso-scale analysis.

	Outer model	**Inner model**	
		NL	**TL/AD**
Horizontal grid spacing	5 km	15 km	
Vertical layers in the atmosphere	76 levels	38 levels	
Vertical layers underground	T_{g}: skin layer + 8 levels, W_{g}: skin layer + 1 level		
Cloud	Six-class three-ice bulk scheme (Japan Meteorological Agency, 2019; Ikuta et al., 2020)		Only the saturation adjustment process is tangent-linearized.
Convection	Kain and Fritsch (1990)		No perturbation
Boundary layer	Mellor-Yamada–Nakanishi–Niino level 3 (Nakanishi and Niino, 2004)		Tangent-linearized except for the diffusion coefficient and the partial condensation
Surface flux	Beljaars and Holtslag (1991)		Tangent-linearized except for the bulk coefficients
Radiation	Japan Meteorological Agency (2019)		Mahfouf (1999)

Table 2. List of abbreviations for observations.

Name	Description
AHI	Advanced Himawari Imager
AIREP	Aircraft Reports
AMDAR	Aircraft Meteorological Data Relay
AMeDAS	Automated Meteorological Data Acquisition System
AMSR2	Advanced Microwave Scanning Radiometer-2
AMSU-A	Advanced Microwave Sounding Unit-A
AMV	Atmospheric Motion Vector
ASCAT	Advanced Scatterometer
ATOVS	Advanced TIROS Operational Vertical Sounder
BUOY	Report of a buoy observation
COSMIC	Constellation Observing System for Meteorology, Ionosphere, and Climate
CSR	Clear Sky Radiance
DMSP	Defense Meteorological Satellite Program
DPR	Dual-frequency Precipitation Radar
GCOM-W	Global Change Observation Mission-Water
GMI	GPM Microwave Imager
GNSS	Global Navigation Satellite System
GNSS-RO	GNSS Radio Occultation
GPM	Global Precipitation Measurement
GRACE	Gravity Recovery and Climate Experiment
GRAS	GNSS Receiver for Atmospheric Sounding
IGOR	Integrated GPS Occultation Receiver
Metop	Meteorological Operational Satellite
NOAA	National Oceanic and Atmospheric Administration
PILOT	Upper-wind report from a land station
R/A	Radar/Raingauge-Analyzed Precipitation
SHIP	Report of surface observation from a sea station
SSMIS	Special Sensor Microwave Imager Sounder
SYNOP	Report of surface observation from a land station
TanDEM-X	TerraSAR-X add-on for Digital Elevation Measurement
TEMP	Upper-level pressure, temperature, humidity, and wind report from a fixed land station
WPR	Wind Profiler

Table 3. Main diffrence of configuration between JNoVA and ASUCA-Var in MA. Note that configuration of LA is different from this table, for example, the basic field update and the VarQC are not used in LA (see subsection 3.2).

	JNoVA	**ASUCA-Var**
Analysis variable	$u, v, P_{\mathrm{s}}, \theta, \mu_{\mathrm{p}}$	$u, v, T_{\mathrm{g}}, P_{\mathrm{s}}, \theta, W_{\mathrm{g}}, \mu_{\mathrm{p}}$
Vertical Background Error	Independent of the location and initial times	Depend on the grid type (land or sea) and initial times (00, 03, 06, 09, 12, 15, 18, and 21 UTC)
Model operator	JMA-NHM	ASUCA
Forward/Backward model	NL/AD	TL/AD
Basic field update	No	2 times
Iteration	35 times	50 times, First loop: 20, Second loop: 15, Third loop: 15
VarQC	Yes, Valid from the 15-th iteration	Yes, Valid from the first iteration
VarBC	No	Yes
Parallell computing	Dividing the domain into strips parallel to the x-direction	Dividing the domain into blocks